Master thesis and internship[BR]- Master's thesis : Numerical simulations of the flow around tandem circular cylinders in the subcritical and postcritical regimes[BR]- Integration internship

Auteur : Martin, Loïc
Promoteur(s) : Andrianne, Thomas
Faculté : Faculté des Sciences appliquées
Diplôme : Master en ingénieur civil en aérospatiale, à finalité spécialisée en "aerospace engineering"
Année académique : 2020-2021
URI/URL : http://hdl.handle.net/2268.2/11564

Liège University
Faculty of Applied Sciences

Numerical simulations of the flow around tandem circular cylinders in the subcritical and postcritical regimes

Author:
Loïc Martin

Academic Supervisor:
Ph.D. Thomas Andrianne

Master thesis conducted for obtaining the Master's degree in Aerospace Engineering

Academic year 2020-2021

“Essentially, all models are wrong,
but some are useful.”

George E. P. Box (1919-2013)

Abstract

As idealized as it may seem, the structures with tandem circular cylindrical profiles are widely found in engineering applications. As the action of the wind does not spare any buildings, the aerodynamic study of these structures is necessary. Therefore, the challenging unsteady flow around smooth and rough tandem cylinders in the subcritical and postcritical regimes is studied through numerical simulations with a rigorous methodology. This thesis aims to assess the ability of 2D URANS simulations to capture the mean and fluctuating quantities and the flow behavior. Experimental data are introduced as principal reference results. The use of wall function boundary conditions is also assessed in both flow regimes, and only very small center-to-center spacings between cylinders are considered.

Two turbulence models are employed in the URANS simulations: the $k-\omega$ SST model and the Langtry-Menter 4-equation Transitional SST model. On the one hand, from preliminary studies, the former model is more suitable for the postcritical regime with wall function boundary conditions. On the other hand, the second model with a resolved viscous layer is more adapted for the subcritical regime as the boundary layer on the upstream cylinder is laminar before separation. For the smooth case, URANS simulations yield very accurate estimations of main quantities in the subcritical regime. In the postcritical regime, the mean flow quantities are captured, and the global wake is narrower as the upstream separation is delayed, which allows using wall functions. The simulations predict the expected shear layer reattachment on the downstream cylinder for both regimes. Regarding roughness, it is only modeled by wall functions. For both regimes, the flow around rough cylinders is simulated thanks to the $k-\omega$ SST model. High discrepancies appear with experimental data for the subcritical regime as wall functions are not adapted for such separated flow. In the postcritical regime, wall functions yield satisfactory results compared to experiments, especially for the upstream cylinder. Notwithstanding the necessary improvements for simulating the flow around rough tandem cylinders in the subcritical regime, the present methodology can be used for further applications on the flow around tandem cylinders.

Acknowledgments

This section is intended to thank those without whom this thesis would not have been possible. First of all, I would like to thank Thomas Andrianne for having proposed this subject and for having continuously followed my work. His advice was invaluable, and I thank him for his support and trust. My thanks also go to Raphaël Dubois for his remarks and the follow-up of my work. I would also like to acknowledge Chandan Bose's help, especially regarding the numerical aspects. His expertise, his experience and his great availability were crucial in this work. I would also like to thank Elena Dislivestro for the follow-up of my work and her more industrial analysis. I am also grateful to the CRM group for the access to the experimental data present in this work.

Finally, I would like to thank my friends for their support and especially a friend with whom I could do a preliminary project that was extremely useful to initiate this thesis. I cannot forget my parents, to whom I dedicate this work, for their absolute comfort and support.

Contents

List of Figures

List of Tables

Nomenclature

Symbol	Description	Units
$()'$	Temporal fluctuating part	-
$()_1$	Reference to upstream cylinder	-
$()_2$	Reference to downstream cylinder	-
$()_f$	Reference to friction part	-
$()_p$	Reference to pressure part	-
Δt	Time-step	s
γ	Intermittency	-
$\mathrm{Re} = \frac{U_\infty D}{\nu}$	Reynolds number	-
$\mathrm{Re}_{\theta \mathrm{t}}$	Transition onset momentum thickness Reynolds number	-
μ_T	Turbulent dynamic viscosity	$\mathrm{m} \cdot \mathrm{kg}^{-1} \cdot \mathrm{s}^{-1}$
ν_T	Turbulent kinematic viscosity	$\mathrm{m}^2 \cdot \mathrm{s}^{-1}$
Ω	Vorticity	s^{-1}
ω	Turbulent specific dissipation rate	s^{-1}
ρ	Air density	$\mathrm{kg} \cdot \mathrm{m}^{-3}$
τ_w	Wall shear stress	$\mathrm{kg} \cdot \mathrm{m}^{-1} \cdot \mathrm{s}^{-2}$
$\mathrm{St} = \frac{fD}{U}$	Strouhal number	-
θ_r	Reattachment angle	deg
θ_s	Separation angle	deg
ε	Turbulent kinetic energy dissipation rate	$\mathrm{m}^2 \cdot \mathrm{s}^{-3}$
C_D	Drag coefficient	-
$C_f = \frac{\tau_w}{0.5 \rho U_\infty^2}$	Skin friction coefficient	-
C_L	Lift coefficient	-
$C_p = \frac{p - p_\infty}{0.5 \rho U_\infty^2}$	Pressure coefficient	-
C_{p_b}	Base pressure coefficient	-
D	Cylinder diameter	m
f	Vortex shedding frequency	s^{-1}
k	Turbulent kinetic energy (TKE)	$\mathrm{m}^2 \cdot \mathrm{s}^{-2}$
K_s	Sand grain roughness	m
L_r	Recirculation region length	m

p_∞	Reference pressure	$\mathrm{kg} \cdot \mathrm{m}^{-1} \cdot \mathrm{s}^{-2}$
S	Center-to-center spacing	m
Tu	Turbulence intensity	-
u^*	Friction velocity	$\mathrm{m} \cdot \mathrm{s}^{-1}$
U_x	Streamwise velocity	$\mathrm{m} \cdot \mathrm{s}^{-1}$
U_y	Vertical velocity	$\mathrm{m} \cdot \mathrm{s}^{-1}$
U_∞	Freestream velocity	$\mathrm{m} \cdot \mathrm{s}^{-1}$
y	Vertical distance from the nearest cylinder wall	m
y^+	Non-dimensional vertical distance (unit wall)	-

Abbreviations

BC	Boundary Conditions
BL	Boundary Layer
CFL	Courant–Friedrichs–Lewy
CPU	Central Processing Unit
DDES	Delay Detached Eddy Simulation
DES	Detached Eddy Simulation
DNS	Direct Numerical Simulation
IC	Initial Condition
IDDES	Improved Delay Detached Eddy Simulation
LCO	Limit Cycle Oscillations
LES	Large Eddy Simulation
LM	Langtry Menter
SST	Shear Stress Transport
URANS	Unsteady Reynolds-Averaged Navier-Stokes
WF	Wall Functions

1. Introduction

1.1. Context

As idealized it seems, the structures with tandem circular cylindrical profiles are enormously found in daily life. To name a few of them, twin chimney stacks, landing gears, pipelines, cables of suspended bridge, cooling tower of nuclear power plant and the Hyperloop project (in progress) are assimilated to a tandem of cylinders. The different applications are illustrated in Figures 1.1, 1.2 and 1.3. They are collected from [1] [2] [3] [4] [5] and [6], respectively. As the action of the wind does not spare any buildings, the aerodynamic study of these structures is necessary. If neglected or wrongly simulated, the wind actions can yield disasters such as failure, which is unacceptable. The example of the oscillating chimney stacks in 2015 at Cornwwall showed such unacceptable structural behavior. As experiments require expensive means, especially to reach flow conditions of the postcritical regime, numerical simulations are carried out to model the wind actions on tandem cylinder structures. As the previously mentioned structures are manufactured with different materials, smooth and rough walls of cylinders are considered to deal with every industrial application.

Figure 1.1: Example of tandem cylinder structures: Cooling towers of nuclear power plant (left) and Landing gears (right).

[1] https://en.wikipedia.org/wiki/Cofrentes_Nuclear_Power_Plant
[2] https://sassofia.com/blog/introduction-to-landing-gear-aircraft-maintenance-management/
[3] https://www.tankstoragemag.com/2020/09/15/rosen-group-developing-hydrogen-pipeline-strategy/
[4] https://www.waters.com/waters/es_MX/Dioxins-and-Furans/nav.htm?cid=134802162&locale=es
[5] https://www.paintsquare.com/news/?fuseaction=view&id=15866
[6] https://www.tesla.com/sites/default/files/blog_images/hyperloop-alpha.pdf


Figure 1.2: Example of tandem cylinder structures: Pipelines (left) and Chimney stacks (right).

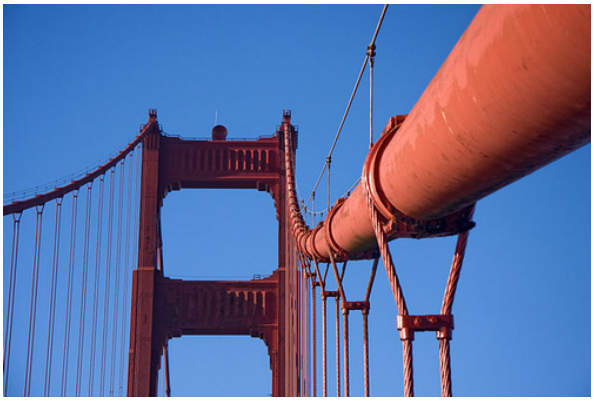
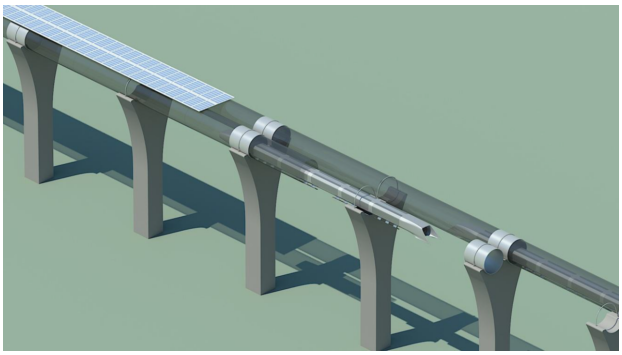

Figure 1.3: Example of tandem cylinder structures: Cables of suspended bridge (left) and Hyperloop project (right).

1.2. Literature

The first experiments focused on the flow around a single-cylinder. Among them, Wieselsberger et al. (1923), Fage and Falkner (1931), Roshko (1961) and Achenbach (1968) experiments are still benchmarks in this domain. The latter extracted data in a wide range of Reynolds number and detailed the boundary layer (BL) behavior regarding transition and separation. He also identified four flow regimes depending on the Reynolds number: subcritical, critical, supercritical, and postcritical. A laminar separation is observed in the first regime, while the same effect is observed in the second and third one but followed by a turbulent reattachment and its associated separation. The latter is delayed and leads to a lower drag coefficient, also called a drag crisis. In the last regime, the transition occurs earlier and leads to a turbulent separation. The impact of roughness on the flow around a single-cylinder has been deeply studied: Fage (1929), Achenbach (1971), Matteoni and Georgakis (2012), Benidir et al. (2015), Van Hinsberg (2015). Achenbach (1971) studied the effect of roughness on the behavior of the BL and discovered that roughness triggers the BL laminar-to-turbulent transition. Compared to smooth cylinders, drag coefficients are much larger as the separation occurs earlier due to BL instabilities. Many numerical simulations were performed. Over the past decades, Unsteady Reynolds-Averaged Navier-Stokes (URANS) simulations such as the ones of Catalano et al. (2003), Ong et al. (2010) and Stringer et al. (2014) succeeded in the estimation of the aerodynamic coefficients for a smooth single cylinder. However, as no transition model was applied, the flow behavior was not correctly approximated. Higher fidelity simulations such as the detached eddy simulations (DES) of Travin et al. (2000) and large eddy simulations (LES) of Catalano et al. (2003) were also performed. The first one showed that for the subcritical regime, DES were much accurate than URANS simulations, while for the postcritical flow, no main difference was observed. Due to limited computational resources, only a few direct numerical simulations (DNS) were performed at a high Reynolds number. The DNS of Dong and Karniadakis (2005) simulated the flow at $\mathrm{Re} = 1 \times 10^4$ and gave correct results for wake behavior and main coefficients. Regarding the simulations of the flow over a rough single-cylinder, Rodríguez et al. (2016) and Han et al. (2021) studies can be highlighted. The former used LES and designed ellipsoid on the surface cylinder, while the latter modified BCs to take roughness into account.

Regarding the flow around tandem cylinders, Zdravkovich (1987) found interest in them and studied the effects of Reynolds and center-to-center spacing. He discovered three flow regimes based on the spacing S/D and depending on the Reynolds number in the subcritical regime. The classical configuration is presented in Figure 1.4. For the spacings such that $0 < S/D <$ 1.2 to 1.8, depending on Re for the upper limit, the separated upstream cylinder shear layers do not reattach on the downstream cylinder. For 1.2 to 1.8 $< S/D <$ 3.4 to 3.8, the separated upstream shear layers reattach on the downstream cylinder, and vortex shedding occurs behind the latter. For $S/D >$ 3.4 to 3.8, alternate vortex shedding occurs behind the upstream and downstream cylinder. In the subcritical regime also, Okajima (1979) and Igarashi (1981) no-

ticed a jump of the drag coefficient and Strouhal number for particular spacing, called critical spacing. The latter depends on the Reynolds number and is around 3.5. After that, Alam et al. (2003) concluded that fluctuating aerodynamic coefficients and fluctuating pressure distribution were very sensitive to the spacing. Their experiment dealt with the flow at $\mathrm{Re} = 6.5 \times 10^4$ with a spacing ranging from 0.1 to 8. A bistable flow was found at $S/D = 3$. They finally showed that phase lag exists between the aerodynamic forces of the two cylinders for $S/D > 3$. Jenkins et al. (2006) studied unsteady flow and wake interference between the two cylinders at $\mathrm{Re} = 1.66 \times 10^5$ with different spacings (1.435 and 3.7). They provided velocity and turbulent kinetic energy (TKE) profiles in the wake. Sumner (2010) achieved an extensive review of all previous studies in the subcritical regime and summarized the entire tandem cylinders literature.

More recently, Schewe and Jacobs (2019) studied the flow behavior around tandem cylinders from the subcritical up to postcritical regimes. They considered a small spacing $S/D = 1.56$ and different attack angles to conclude the structural stability of tandem cylinder configuration. At zero angle of attack, the drag coefficient of the upstream cylinder behaves as for the single-cylinder, while the drag coefficient of the downstream cylinder resembles the inverse of the former. The upstream drag second inversion coupled with structure topology changes in the postcritical regime can cause instability. The experimental literature suffers from the lack of roughness impact study on the flow around tandem cylinders. However, recently, Dubois and Andrianne (2021) considered highly rough ($K_s/D = 7.2 \times 10^{-3}$) tandem of cylinders at $\mathrm{Re} = 4.5 \times 10^4$ and 3.95×10^5. Their combination of roughness and the considered Reynolds numbers allows considering the subcritical and postcritical flow regimes. Indeed, the roughness promotes the laminar-to-turbulent transition and consequently yields a lower critical Reynolds number where drag crisis occurs.

Regarding numerical simulations of the flow around tandem cylinders, Garbaruk et al. (2010) used delayed detached eddy simulations (DDES) and improved delayed detached eddy simulations (IDDES) at $\mathrm{Re} = 1.66 \times 10^5$ with $S/D = 3.7$. They concluded that both methods yielded quite similar results and were in good agreement with experimental data. However, they have higher hopes in IDDES for the future. Uzun and Hussaini (2012) simulated the flow around a tandem of cylinders at $\mathrm{Re} = 1.65 \times 10^5$ thanks to DDES. They observed satisfactory agreement with experiments, but they faced turbulence modeling uncertainty and limited spanwise extension. Weinmann et al. (2014) introduced a URANS-LES hybrid method to model the flow around a tandem of a smooth cylinder at $\mathrm{Re} = 1.66 \times 10^5$ and with $S/D = 3.7$. The SST-based turbulence model agreed the best with experimental data regarding the hydrodynamic field from their model comparison. In the context of hydraulic power extraction, Derakhshandeh et al. (2014) modeled the vortex-induced vibrations (VIV) due to the flow around a tandem of cylinders at $\mathrm{Re} = 6.5 \times 10^4$ by using SAS (Scale-Adaptive Simulations). They studied different spacings and relative positions for both cylinders and concluded that the latter highly influenced the VIV efficiency. Gopalan and Jaiman (2015) introduced non-linear hybrid URANS-

LES method to model the flow at Re $= 1.66 \times 10^5$ with $S/D = 1.4$, 3 and 3.7. They observed the different flow behaviors expected by Zdravkovich (1987) and induced by the change of the spacing. They also observed a bi-stable shedding mode for $S/D = 3$. More recently, Hu et al. (2019) performed IDDES at Re $= 2.2 \times 10^4$ and Re $= 3 \times 10^6$. The non-dimensional spacing was varied from 2 to 5. Among others, they observed lower aerodynamic fluctuations when the Reynolds number was increased.

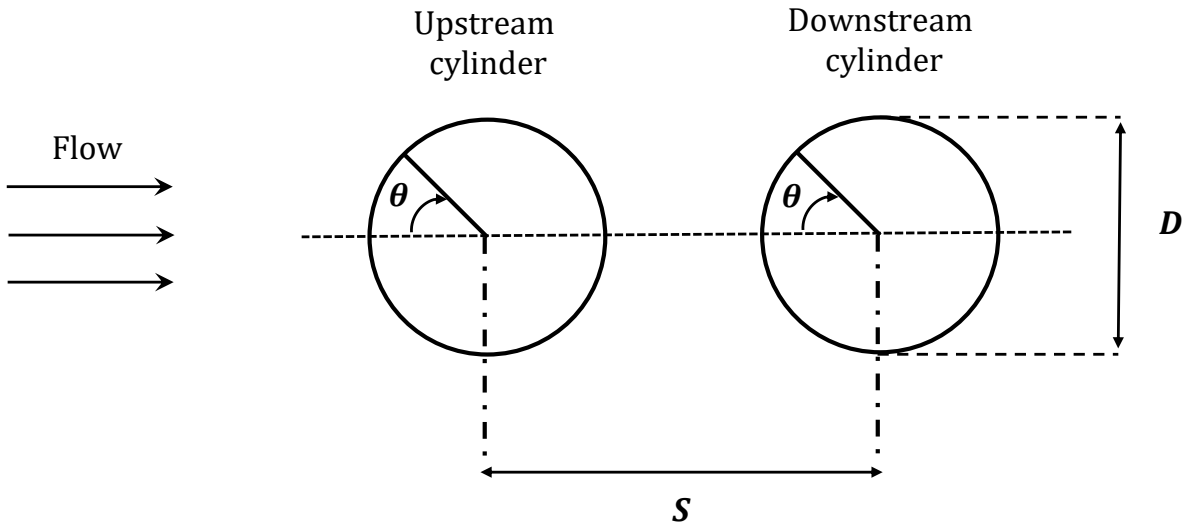

Figure 1.4: Tandem cylinders configuration subject to a cross flow.

1.3. Objectives

The present thesis aims to simulate the flow around two aligned identical static cylinders in a tandem configuration. Smooth and rough cylinders are considered. Very small center-to-center spacings are considered and both the subcritical and postcritical flow regimes are analyzed. Given the lack of URANS simulations in the numerical literature for the flow around a tandem cylinder and in the research of compromise between accuracy and computational cost reduction, this thesis aims to assess the capability of the URANS formulation to capture the mean and fluctuating aerodynamic coefficients, the pressure distributions and the wake behavior compared to experimental results. The use of wall function boundary conditions is also assessed.

The thesis is organized as follows. Section 2 introduces the general methodology employed in the simulations and selects the best models. Then, Section 3 validates the selected models by simulating the flow around smooth tandem of cylinders. After that, Section 4 presents several results regarding the Reynolds effects in the subcritical regime, the roughness effects in both regimes, and the different flow topologies. Finally, Section 5 summarizes the main conclusions and presents perspectives for future works.

2. Methodology

This section describes the general computational methodology adopted in the present simulations. First, the mathematical formulations of the two different URANS models and the wall function boundary conditions for smooth and rough walls are presented. The numerical aspects of the simulations, such as computational domain, solver parameters, and boundary conditions are depicted. Then, the efficacy of turbulence modeling in the subcritical and postcritical regimes is assessed by simulating the flow around a single-cylinder.

2.1. Mathematical models

The 2D incompressible Unsteady Reynolds-Averaged Navier-Stokes (URANS) equations are given by

$$\begin{aligned} &\frac{\partial u_i}{\partial x_i} = 0 \\ &\frac{\partial u_i}{\partial t} + u_j \frac{\partial u_i}{\partial x_j} = -\frac{1}{\rho}\left(\frac{\partial P}{\partial x_i}\right) + v\frac{\partial^2 u_i}{\partial x_j^2} - \frac{\partial \overline{u_i' u_j'}}{\partial x_j}. \end{aligned} \tag{2.1}$$

These three equations, one for mass and two for 2D momentum conservations respectively, lack closure due to the Reynolds stress components: $\overline{u_i' u_j'}$. Using the Boussinesq approximation:

$$\overline{u_i' u_j'} = -\nu_T \left(\frac{\partial u_i}{\partial x_j} + \frac{\partial u_j}{\partial x_i}\right) + \frac{2}{3} k \delta_{ij}, \tag{2.2}$$

the Reynolds stresses can be modeled invoking the turbulent viscosity. The latter is computed using URANS models by incorporating new equations to achieve closure in the governing equations system.

Two well-known URANS models are used in this work. They allow considering different BL behaviors. The first URANS model used in this work is the $k-\omega$ SST. Introduced by Menter (1994), this two-equation model (for k and ω) combines two of the previous two-equations turbulence models: the $k-\varepsilon$ described by Jones and Launder (1972) and the $k-\omega$ introduced by Wilcox (1988). The $k-\omega$ model is used in the inner part of the boundary layer while it switches to the $k-\varepsilon$ formulation in the region of the freestream layers. This switch eliminates the high sensitivity of the model to freestream conditions. It also provides physical results against turbulence anisotropy and adverse pressure gradient, which are often essential to capture while dealing with flows around cylinders.

The second employed model is the Langtry-Menter 4-equation Transitional SST Model introduced by Langtry (2006) and Langtry and Menter (2009). This model aims to capture the laminar-to-turbulent transition, which is critical to model, especially in the subcritical regime, see Cousteix (2003). Based on the $k-\omega$ SST closure, this model is also called $\gamma - \mathrm{Re}_{\theta_t}$ due to

the two supplementary equations: one for the intermittency (γ) and the other for the transition momentum onset thickness Reynolds number (Re_{θ_t}). The BL is considered as laminar when $\gamma = 0$ and turbulent for $\gamma = 1$. From Langtry (2006), it is known that this model is more sensitive to freestream conditions compared to the $k - \omega$ SST model.

2.2. Numerical aspects

Solver parameters

Assuming the two-dimensional nature of the flow-structures, 2D URANS simulations are performed. Indeed, no many 3D simulations are performed due to prohibitive computational cost. The flow is solved using the open-source library OpenFOAM v2006 (OpenFOAM, 2020). Following Hirsch (2007), assuming the flow to be 2D, incompressible and turbulent, the `pisoFoam` solver is used. The URANS equations are solved based on the PISO (Pressure-Implicit with Splitting of Operators) algorithm proposed by Issa (1986). Three `nCorrectors` (PISO loop correction) are employed to solve the pressure equation with sufficient accuracy. Additionally, three `nNonOrthogonalCorrectors` account for the mesh non-orthogonality induced by the unstructured mesh region around the two-cylinder boundary layers. As explained by Gopalan and Jaiman (2015), an adaptive time-step based on the definition of a maximum CFL number is suitable for simulating transient flows. However, the original version of the `pisoFoam` solver does not integrate this option. This option has been implemented to allow this time-step adaptation, ensuring a stable solution and reducing the computational cost.

Unsteadiness of the flow requires high precision and low dissipation for the time integration, see Hirsch (2007). Therefore, the second-order, implicit, bounded Crank-Nicolson scheme is chosen. The equations are discretized using Gaussian finite integration. Limited second-order schemes are introduced for advective terms as a compromise between accuracy and stability. The preconditioned bi-conjugate gradient algorithm solves the algebraic equations for pressure, and its stabilized variant solves the other quantities equations. The pressure and all transport quantities are considered converged when residuals reach 10^{-8} for absolute tolerances and 0 for relative tolerances. These high requirements are necessary for unsteady flow simulations, especially for the pressure-velocity coupling (OpenFOAM, 2020).

Computational domain

The computational domain of the simulation of the flow around the tandem cylinders is presented in Figure 2.1. It has a dimension of $20D$ along the y-direction for width and $30D$ along the x-direction from the center of the downstream cylinder. Dimensions and the rectangular shape are chosen by following previous numerical simulation recommendations: Gopalan and Jaiman (2015) and Hu et al. (2019). Hemi-circular inlets exist, as in the simulations of Weinmann et al. (2014), but are not often used. With these recommended dimensions, the boundary

effects are eliminated by applying appropriate BCs. The domain size is kept constant irrespective of the flow regime (subcritical and postcritical). The only change affecting the domain is the center-to-center cylinder spacing S. The axes origin $(0, 0)$ is placed at the centerline between the two cylinders, which are aligned and have the same diameter.

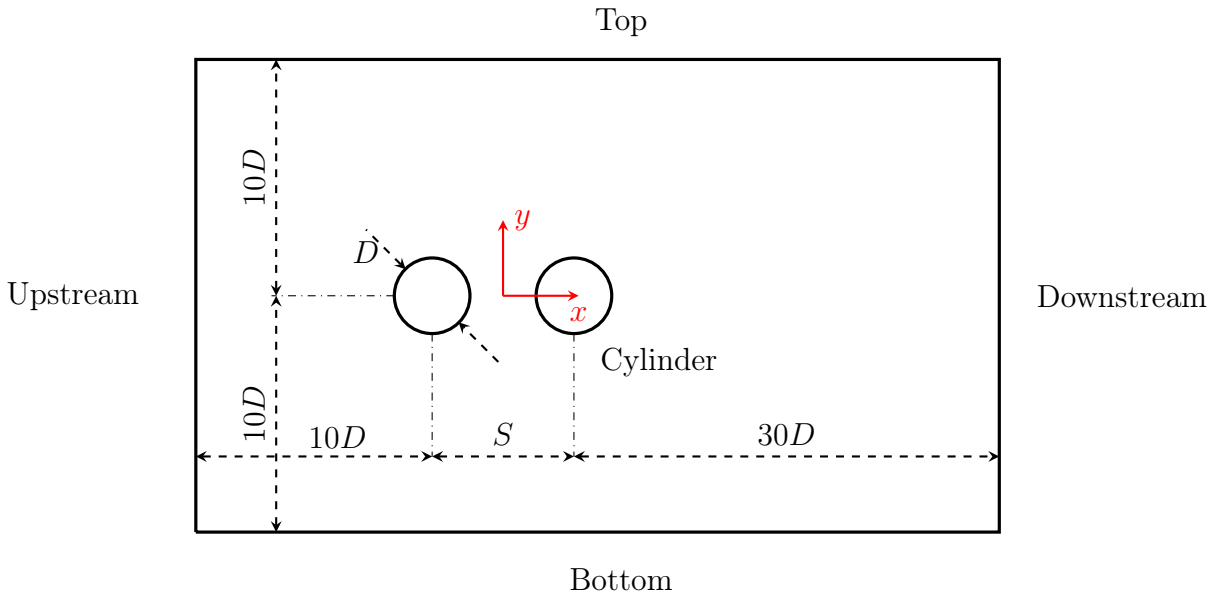

Figure 2.1: Computational domain of the flow around tandem cylinders (not to scale).

Boundary conditions

Referring to Figure 2.1, appropriate boundary conditions are prescribed at the four surrounding surfaces (upstream, downstream, top and bottom) and at cylinders surface. The boundary conditions are critical from the viewpoint of the accuracy of the results. For the $k-\omega$ SST model, they must be attributed at each surface for the following quantities: $\mathbf{u}$ (velocity), p (pressure), k (turbulent kinetic energy), ω (specific turbulent dissipation rate) and $\nu_\mathrm{t} = k/\omega$ (eddy viscosity). If the transition model ($\gamma - \mathrm{Re}_{\theta\mathrm{t}}$) is considered, two additional quantities must be defined at each boundary surface: γ (intermittency) and $\mathrm{Re}_{\theta\mathrm{t}}$ (transition onset momentum thickness Reynolds number).

(i) At the inlet, a uniform cross-flow along x-axis is chosen such that:

$$\mathbf{u} = U_\infty \mathbf{e_x}. \tag{2.3}$$

The freestream turbulence intensity is set according to reference experimental data. If this information is missing, it is assumed to be of the same order of magnitude compared to other experiments. The freestream turbulence intensity affects the inlet k value, as can be seen in

Equation 2.4.

$$k_{\text{inlet}} = \frac{3}{2}(U_\infty \cdot Tu)^2. \tag{2.4}$$

From this value, the ω value at inlet can be computed following Equation 2.5.

$$\omega_{\text{inlet}} = \frac{k_{\text{inlet}}^{0.5}}{C_\mu^{0.25} L_{\text{t}}}, \tag{2.5}$$

where the empirical constant C_μ is fixed at 0.09 and L_{t} is a turbulent length scale. L_{t}/D is typically around 0.07 for external flows around cylinder, see Stringer et al. (2014). Other formulations exist for ω at inlet, such as the formulation of Langtry (2006):

$$\omega = \frac{k}{\beta\nu}, \tag{2.6}$$

where $\beta = \nu_t/\nu$ is the turbulent viscosity ratio. Note that Equation 2.5 is used throughout the present investigation. For the two additional quantities of the transition model ($\gamma - \text{Re}_{\theta\text{t}}$), the intermittency γ was prescribed to unity by Langtry and Menter (2009) such that the original freestream turbulence decay rate is preserved. The two authors recommend the following formulas for $\text{Re}_{\theta\text{t}}$ at the inlet, where Tu is expressed as a percentage.

$$\text{Re}_{\theta\text{t}} = \begin{cases} 1173.51 - 589.428 \cdot Tu + \frac{0.2196}{Tu^2} & \text{if } Tu \leq 1.3, \\ 331.5[Tu - 0.5658]^{-0.671} & \text{if } Tu > 1.3. \end{cases} \tag{2.7}$$

(ii) As explained in Section 2.2, the boundaries have been chosen sufficiently far away from the cylinder walls. Therefore, the top and bottom boundaries are assigned slip conditions for velocity. Other choices exist for BCs in these regions, such as freestream conditions but do not affect the solution. All other transport variables are assigned a normal zero gradient.

(iii) The outlet pressure is set to zero at the downstream and is assigned zero gradients everywhere else (Neumann boundary condition). Also, at the downstream, all other transport variables are assigned zero gradient boundary conditions.

(iv) No-slip condition is applied at the cylinder walls. This leads to zero velocity $\mathbf{u}$, and as k is linked to the turbulent velocity, its value must also be zero at the cylinder wall. Nonetheless, its value is set around 10^{-10} to avoid numerical instability. Regarding ω, Menter (1994) recommended the following formula:

$$\omega_{\text{wall}} = \frac{60\nu}{0.075 y_1^2}, \tag{2.8}$$

where y_1 is the distance from the wall to the first node.

The use of wall functions is another way to prescribe boundary conditions at walls, allowing the first cells near the wall to be in the log-layer ($30 < y^+ < 200$) instead of the viscous sublayer ($y^+ < 5$). This reduces the computational cost considerably and allows less stiff computations, see Kalitzin et al. (2005). Furthermore, WF BCs offer a very compact way to model roughness. Liu (2016) thoroughly described how wall functions were implemented and worked in OpenFOAM, giving the following relations for turbulent quantities at the wall depending on the value of y^+:

$$\nu_{t_{\text{vis}}} = 0, \quad \nu_{t_{\text{log}}} = \nu\Big(\frac{y^+\kappa}{\ln(Ey^+)} - 1\Big), \qquad \omega_{\text{vis}} = \frac{6\nu}{\beta_1 y^2}, \quad \omega_{\text{log}} = \frac{k^{0.5}}{C_\mu^{0.25}\kappa y}, \tag{2.9}$$

where κ is the von Kármán constant, $\beta_1 = 0.075$ and $E = 9.8$. ν_t and ω are blended according to a binomial law by default, allowing to deal with cells in the buffer and viscous layers. Regarding k, it is assigned zero gradients.

An easy way to model rough walls is to use the relations of wall function BCs in Equation 2.9 and slightly change them by modifying the turbulent viscosity value. This change has been described by Nikuradse et al. (1950) and is given in Equation 2.10.

$$\nu_{t_{\text{log}}} = \nu\Big(\frac{y^+\kappa}{\ln(E'y^+)} - 1\Big), \quad E' = \frac{E}{\exp(\Delta B)}, \tag{2.10}$$

where

$$\begin{aligned}
&\Delta B = 0 \quad \text{if} \quad K_s^+ < 2.25, \\
&\Delta B = \frac{1}{\kappa}\ln\left(\frac{K_s^+ - 2.25}{87.75} + C_s K_s^+\right) \cdot \sin\left(0.4258\left[\ln K_s^+ - 0.811\right]\right) \quad \text{if} \quad 2.25 < K_s^+ < 90, \\
&\Delta B = \frac{1}{\kappa}\ln\left(1 + C_s K_s^+\right) \quad \text{if} \quad K_s^+ > 90,
\end{aligned} \tag{2.11}$$

with

$$K_s^+ = \frac{\rho K_s u^*}{\mu}. \tag{2.12}$$

Therefore, to model roughness at walls, two parameters must be provided by the user: the sand grain height (K_s [m]) and the uniformity of the sand grain roughness (C_s [-]). Roughness is considered uniform when $C_s = 0.5$.

Initial conditions

While the boundary conditions (BC) are critical, initial conditions (IC) do not affect the solution. A transient solution develops and leads to limit cycle oscillations (LCOs) in aerodynamic coefficients. For the first simulations, ICs were chosen as upstream boundary conditions. When convergence studies are performed, final solutions are mapped onto finer mesh thanks to `mapFields` facility.

Mesh description

The spatial discretization of the domain is achieved using a hybrid mesh as an assembly of structured and unstructured blocks. Three main zones are considered:

- **Boundary layers** As prescribed by Hirsch (2007), the boundary layers are composed of structured hexahedral cells with radial refinement through the cylinders. This mesh region is represented in Figure 2.2(c). This refinement is necessary to capture large changes and gradients due to boundary layer development. The first grid cell (near the wall) must have a $y^+ \approx 1$ for resolving the viscous layer and such that $30 > y^+ > 200$ when wall treatment is applied. As the y^+ value is known after the post-processing of results, an iterative process is performed to find the correct value of the first cell height y_1. Relations in Equation 2.13 and skin friction empirical formula from Schlichting and Gersten (1979) allows to get an initial guess of y_1 and to converge to acceptable values of y^+ at the wall proximity. As the skin friction coefficient depends on the Reynolds number, the radial refinement will change according to the studied flow regime.

$$y^+ = \frac{yu^*}{\nu}, \quad u^* = \sqrt{\frac{\tau_w}{\rho}}, \quad \tau_w = \mu\left(\frac{\partial u}{\partial y}\right)_{y=0} = C_f \frac{1}{2}\rho U_\infty^2. \tag{2.13}$$

  A bump or double progression is applied to the back face of the upstream cylinder and the front and back faces of the downstream cylinder to correctly capture wake topology.

- **Cylinder Boundary layers surrounding** This unstructured mesh region, represented in Figure 2.2(b), covers the two boundary layers of the cylinders and is helpful to build a rectangular zone around them. It is composed of prismatic cells, which are more convenient than hexahedra for unstructured blocks following Owen (1998). This unstructured region serves as a smooth transition between boundary layers and the vast surrounding, which is structured.

- **Inlet, surrounding and outlet** These far-field zones, in Figure 2.2(a), are composed of structured hexahedral cells. These mesh regions do not require too many cells as a radial refinement is performed. A smooth transition between structured and unstructured zones is preserved. A double regression is applied to the outlet region to capture vortex shedding and wake topology.

As the radial requirements are previously met (acceptable range for y^+), the mesh convergence study in Section 3.1 is only based on the refinement along the azimuthal direction. The number of elements along the cylinders' surfaces and the surroundings will be increased until the solution becomes mesh independent.

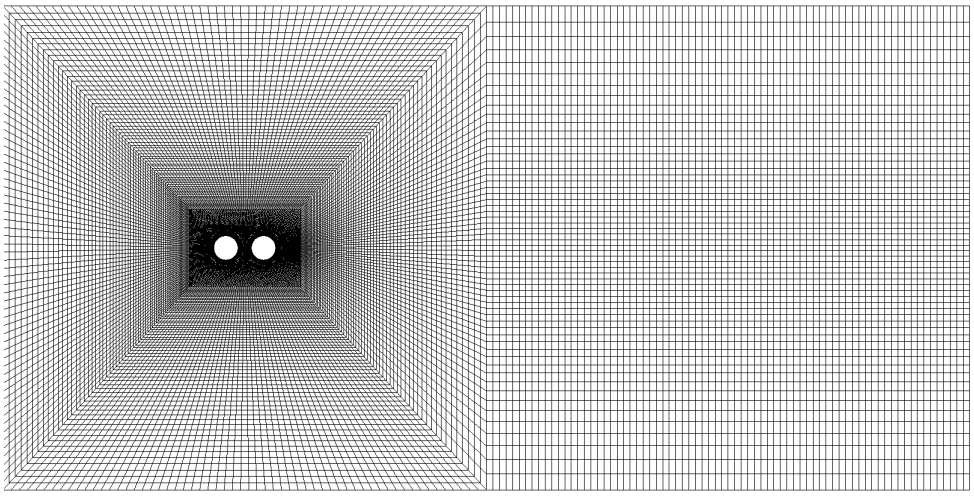

(a) Chosen mesh for the entire domain

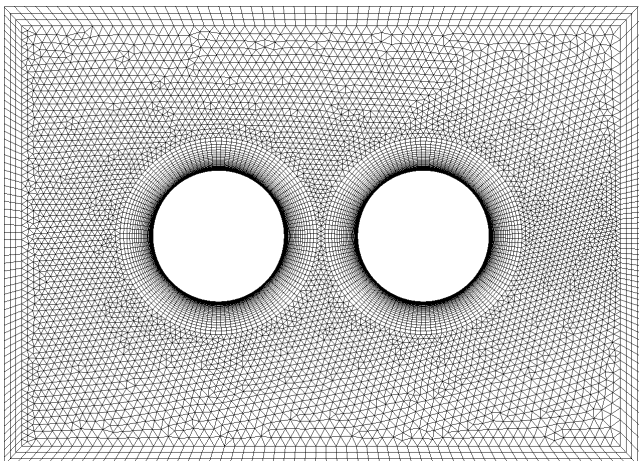

(b) Close-up on the unstructured surrounding

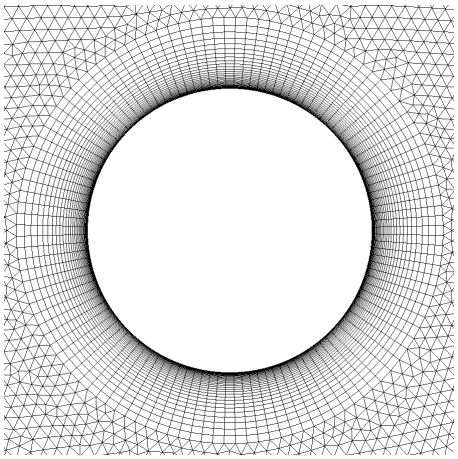

(c) Close-up on the upstream cylinder

Figure 2.2: Hybrid mesh combining structured and unstructured discretizations.

Adaptive time-stepping

To maintain a balance between stability, precision, and optimization of the computing time, the source code of `pisoFoam` has been adjusted to allow the dynamic change of the time step $\Delta t U_\infty / D$. The latter is increased while the maximum CFL number does not exceed a critical threshold value based on the studied problem. Firstly, the maximum CFL is set to 0.9 and is further decreased to achieve the temporal convergence in Section 3.1. The use of wall functions and the considered flow regime affect the choice of the maximum CFL number.

Computational resources

The simulations have been performed by using parallel computations on the cluster *NIC5* of CECI (2021) to tackle the need for high computational time, especially in the postcritical flow regime. The domain is divided into 32 or 48 sub-domains in a simple way, for the subcritical and postcritical regimes, respectively.

2.3. Assessment of the best modeling

This section focuses on the validation of the solver parameters and the boundary conditions and the assessment of the best modeling approach for both the subcritical and postcritical regimes for a smooth single-cylinder. The single-cylinder configuration is studied as more evident conclusions can be drawn from its analysis. To do so, the flow around a smooth single-cylinder is studied at $\mathrm{Re} = 1 \times 10^5$ and 5×10^6. In the subcritical regime, the impact of transition model and wall functions is studied, while in the postcritical regime, where the laminar-to-turbulent transition occurs near the stagnation point, only the $k - \omega$ SST model is employed. For the latter, the impact of wall functions is investigated.

Following previous recommendations from the past numerical studies: Ong et al. (2010), Rosetti et al. (2012) and Zhang et al. (2014), the computational domain of the single-cylinder is chosen similar to that of the tandem cylinders case (*cfr.* Figure 2.1). The domain size remains the same irrespective of whether the flow regime is subcritical or postcritical. The boundary conditions and the solver set-up remain unchanged. However, as the geometry is simpler than the tandem cylinders, the entire domain is discretized with structured hexahedral cells with radial refinement near the boundary layer. The transition model is adopted for the same mesh as the classical $k-\omega$ SST model. The adaptive time-step is also considered for the single-cylinder case.

Mesh and time convergence studies have been performed to minimize numerical errors in evaluating the best model. An example is given in Figure 2.3 for subcritical case without wall functions. From this figure, the number of cells and the maximum CFL number are chosen such that the relative error does not exceed 1% when further increasing the number of cells or decreasing the maximum CFL number. The summary of the number of cells and maximum CFL number for both regimes is presented in Table 2.1. The maximum allowed CFL number is higher when wall treatment is applied. Also, as a result, the required number of cells is higher for the postcritical regime and higher if the wall is resolved. Finally, y^+ ranges have been validated for the two regimes, as confirmed by Figure 2.4.

The two regimes are then studied separately to define the best modeling clearly. The mean and fluctuating force coefficient, the Strouhal number, the mean pressure, and the skin friction coefficient distributions are compared to Achenbach (1968) and Roshko (1961) when available for both regimes. It must be mentioned that the main limitation of Achenbach (1968) experiment is that no one result was corrected while they should have been corrected due to the high blockage ratio: around 16 %.

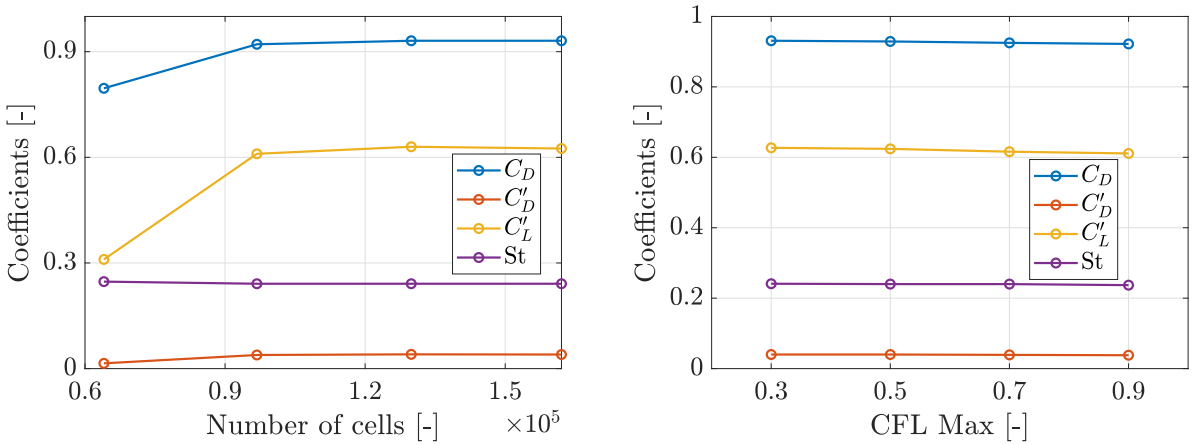

(a) (b)

Figure 2.3: Mesh and CFL convergence studies for the subcritical flow regime without wall functions for a single-cylinder.

	WF sub.	No WF sub.	WF post.	No WF post.
Cells	9×10^4	1.3×10^5	1.22×10^5	2.34×10^5
CFL Max [-]	0.9	0.7	0.9	0.7

Table 2.1: Summary of the required number of cells and the maximum CFL number [-] for the subcritical and postcritical regimes with and without wall functions.

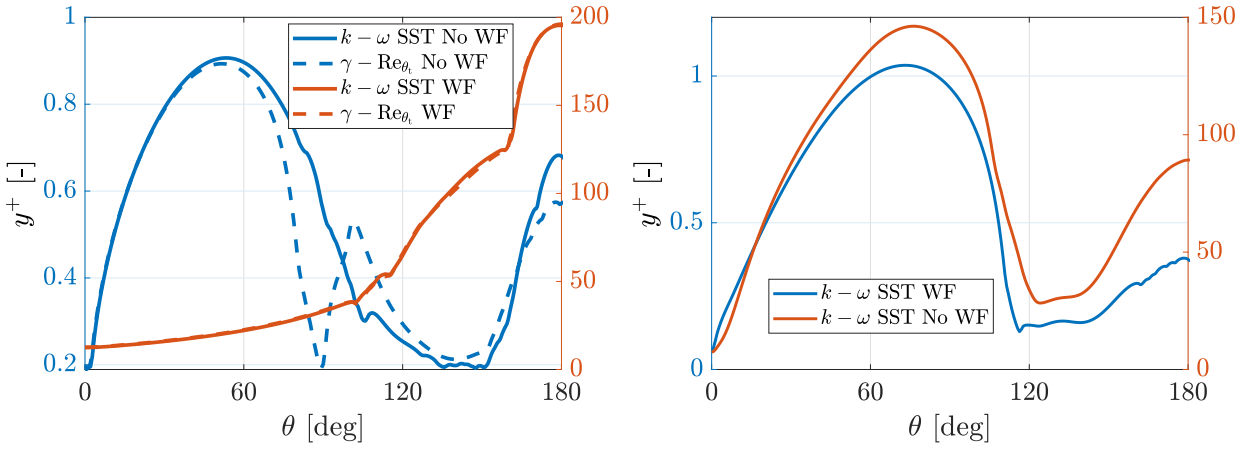

(a) Subcritical (b) Postcritical

Figure 2.4: y^+ distribution over the cylinder for the two regimes. Four cases for subcritical and two cases for postcritical.

Subcritical regime

Table 2.2 summarizes the mean and fluctuating coefficient for the four cases in the subcritical regime. As a first remark, Langtry and Menter (2009) noticed that y^+ at the first cell should be lower than 1 to capture the transition. This remark explains why the wall function associated with the transition model does not induce any change compared to the classical $k-\omega$ SST model with wall functions. Differences are more visible between the two models without wall function, where the transition model seems to provide better estimations of the main coefficients. High discrepancies can be observed between the resolved wall and the wall function cases. For the wall functions, the separation angle and the drag coefficients are vastly overestimated compared to Achenbach (1968). The overestimation of the drag mainly comes from the inaccurate estimation of the base pressure in Figure 2.5(a) and the wrong estimation of the flow separation angle. Furthermore, the skin friction distribution differs from the experimental one. The wall functions are not adapted for highly separated flow as reported by Kalitzin et al. (2005). The subcritical flow around a single-cylinder seems to present a too large separation to be modeled with wall functions.

Coeff.	$k-\omega$ SST WF	$\gamma - \mathrm{Re}_{\theta_t}$ WF	$k-\omega$ SST No WF	$\gamma - \mathrm{Re}_{\theta_t}$ No WF	Achenbach (1968)
Mean					
C_D [-]	1.51	1.51	0.95	0.93	1.24
θ_s [deg]	111	111	100	88	78
St [-]	0.29	0.29	0.26	0.24	0.2
Fluctuating					
C'_D [-]	0.143	0.14	0.04	0.06	-
C'_L [-]	0.98	1	0.78	0.62	-

Table 2.2: Impact of the transition model and wall functions in the subcritical regime for a single-cylinder. Main coefficients are compared to results of Achenbach (1968) when available.

Regarding the resolved cases (without wall functions), the transition model gives more precise estimations of the main coefficients and the separation angle, with still differences attributed to 3D effects. After that, the transition model matches experimental data well for the skin friction coefficients and pressure distribution. Some differences still exist between the experiment and transition model, but the same physics is captured, i.e., a laminar separation of the boundary layer of the front face of the cylinder. The transition model is necessary because the BL must be considered as laminar at this Reynolds number. The resolved classical $k-\omega$ SST model provides satisfying results but misses the laminar behavior of the BL by assuming a turbulent

boundary layer which induces a delay in the separation. This wrong flow modeling slightly affects the aerodynamic coefficients.

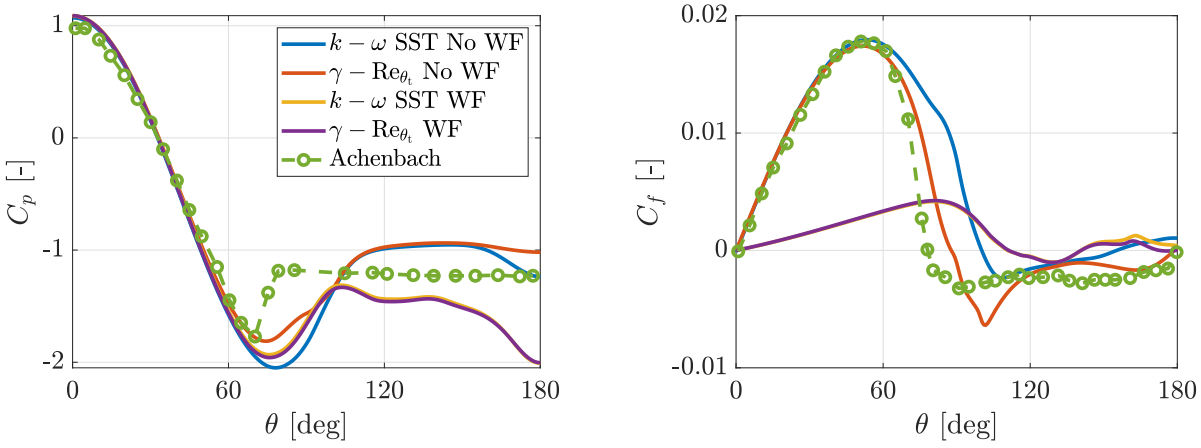

(a) (b)

Figure 2.5: Impact of the wall functions and the transition model on time-averaged pressure and skin coefficients. All URANS results are compared to Achenbach (1968) at $\mathrm{Re} = 1 \times 10^5$.

Postcritical regime

In the postcritical regime, only the $k-\omega$ SST model is used with a wall treatment and a resolved viscous layer. Table 2.3 summarizes the mean and fluctuating aerodynamic coefficients, the Strouhal number, and the separation angle for the two present URANS cases and the experimental data. Mean pressure and friction coefficient distributions are presented in Figure 2.6. As a first conclusion, wall functions do not induce significant changes compared to the wall-resolved case for this flow regime. By analyzing the experimental data, URANS simulations underestimate the mean drag coefficient. This can be explained by Figure 2.6(a), where the base pressure is also underestimated compared to Achenbach (1968) and Roshko (1961) data. The angle of separation and the allures of C_f in Figure 2.6(b) are well approximated by both the URANS simulations, while the amplitude of C_f is less accurately estimated. It seems that at a very high Reynolds number, the wall functions can capture the main physics. The flow is less separated due to the delay in the angle of separation, leading to a narrower wake. Also, the fluctuating aerodynamic coefficients at $\mathrm{Re} = 5 \times 10^6$ are lower than in the subcritical regime.

Figure 2.7 presents instantaneous vorticity contours along the z-axis for both regimes, simulated with the best modeling. 44 values of vorticity going from -550 to 550 with an exponential distribution are represented. It can be quickly observed that the separation occurs earlier and that the wake is wider for the subcritical than the postcritical regime. Also, as the Strouhal number is slightly higher in the postcritical regime than in the subcritical regime, more vortices are shed by a unit of time.

Coeff.	$k-\omega$ SST WF	$k-\omega$ SST No WF	Achenbach (1968)	Roshko (1961)
Mean				
C_D [-]	0.49	0.49	0.71	0.70
θ_s [deg]	112	115	115	-
St [-]	0.27	0.31	-	0.26
Fluctuating				
C'_D [-]	0.015	0.018	-	-
C'_L [-]	0.28	0.27	-	-

Table 2.3: Impact of wall functions in the postcritical regime for a single-cylinder. Main coefficients are compared to postcritical results of Achenbach (1968) and Roshko (1961) when available.

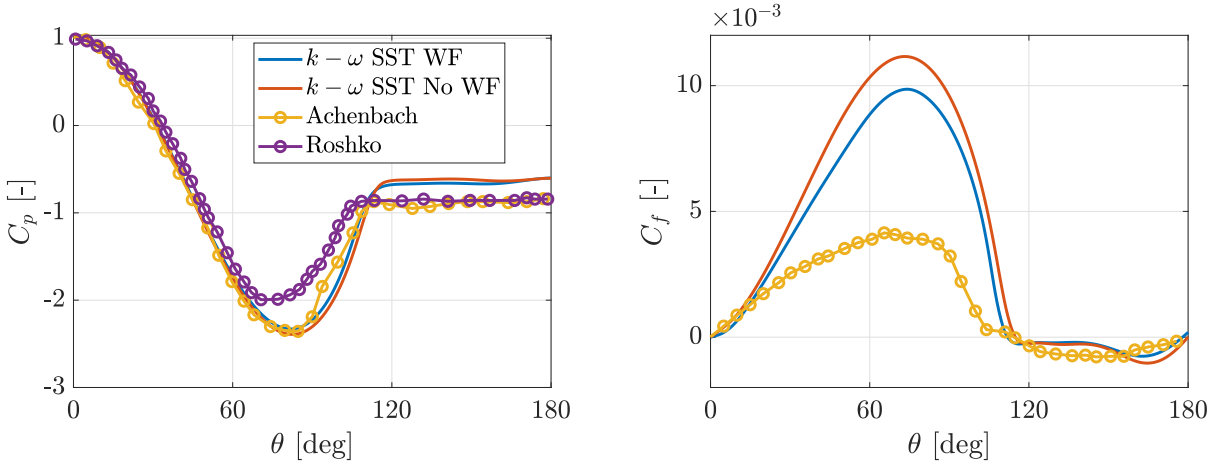

(a) (b)

Figure 2.6: Impact of wall function on time-averaged pressure and skin coefficients. Present simulations are compared to Achenbach (1968) at $\mathrm{Re} = 3.6 \times 10^6$ and Roshko (1961) at $\mathrm{Re} = 8.4 \times 10^6$.

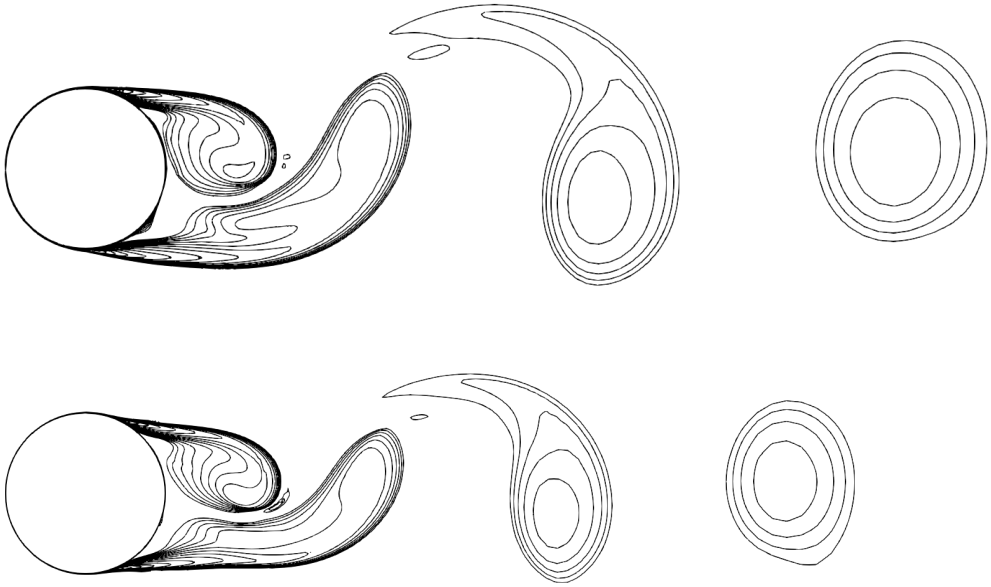

Figure 2.7: Instantaneous vorticity contours for a single-cylinder in the subcritical and the postcritical regimes.

Conclusions

In the subcritical regime, the flow around smooth tandem cylinders will be modeled by the $\gamma - \mathrm{Re}_{\theta_t}$ model without wall function. In this regime, the boundary layer must be considered as laminar before separation. Regarding the postcritical regime, as the use of wall functions does not alter the results and leads to lower CPU resources, see Table 2.4, the wall functions are selected for the study of the postcritical regime. Furthermore, the transition model does not have any impact such that the classical $k - \omega$ SST model is selected. In the postcritical regime, the use of wall functions has an impact as CPU resources are divided by a factor of 8 compared to the wall-resolved case. The factor drops to 2.25 in the subcritical regime, making wall functions less vital at a lower Reynolds number. Finally, as roughness requires wall functions, the use of the transition model when considering rough walls is disregarded due to its incompatibility with wall functions according to Langtry and Menter (2009). Hence, only the $k - \omega$ SST model will be used to simulate the flow around rough cylinders. Prudence in the analysis of rough cylinders will be necessary, particularly in the subcritical flow regime as wall functions presented bad results in that Reynolds range.

Regime	Wall function	No wall function
Subcritical	4	9
Postcritical	10	80

Table 2.4: Impact of wall functions on CPU [core-hour]. 5 seconds of steady LCO were simulated with converged mesh and CFL number (*cfr.* Table 2.1).

3. Model validation

In this section, the temporal and spatial convergence studies of the selected models are performed. After the numerical independence of the solution, both models are applied to their appropriate flow regime for smooth tandem cylinders, i.e., the $\gamma - \mathrm{Re}_{\theta_t}$ model without wall function for the subcritical flow and the $k-\omega$ SST model with wall function for the postcritical regime. The objective is to validate the selected URANS model by comparing simulation results to the available experimental data. Small center-to-center spacings S are considered such that the tandem cylinders behave nearly as a single bluff body. The subcritical computations simulate the experiments of Alam et al. (2003) and Schewe and Jacobs (2019) while the postcritical computations focus only on Schewe and Jacobs (2019) experiments. The experiment of Alam et al. (2003) presents mean and fluctuating pressure and aerodynamic coefficients, while the second experiment has examined a very high Reynolds number but only provides mean coefficients. Mean, and fluctuating pressure distributions, velocity, and TKE distributions measured by Jenkins et al. (2006) are considered as references to compare with the subcritical simulated case. Indeed, the latter considered the same kind of experiments as Schewe and Jacobs (2019) and Alam et al. (2003), i.e., small spacing and the subcritical flow regime. Table 3.1 summarizes the parameters of the three experiments.

Parameters	Alam et al. (2003)	Schewe and Jacobs (2019)	Jenkins et al. (2006)
Re [-]	6.5×10^5	1.66×10^5 & 5×10^6	1.66×10^5
S/D [-]	1.3	1.56	1.435
Tu [%]	0.19	0.4	0.09

Table 3.1: Parameters of experimental literature for tandem cylinders.

3.1. Convergence of the selected models

The spatial and temporal convergence studies (*cfr.* Section 2.2) are carried out to ensure the numerical accuracy of the solution. Given the flow unsteadiness, time-averaged, fluctuating force coefficients and the Strouhal number are computed. The Strouhal numbers of the upstream and downstream cylinders are very similar such that only the Strouhal number associated with the downstream cylinder is presented. Lift coefficients of both cylinders oscillate, but vortex shedding only occurs behind the downstream cylinder. A mesh and a maximum CFL number are considered valid when the relative error between two successive quantities does not exceed 1 %. Figures 3.1 and 3.2 show a convergence study example for the simulation of Alam et al. (2003) experiment. Furthermore, y^+ ranges have been validated for each case. Main CFD parameters, including the number of cells and the maximum CFL number, are summarized

in Table 3.2 for each experiment simulation. The CPU is based on the required resources to simulate 5 seconds of steady LCO with converged mesh and CFL number. As it can be seen for the postcritical case, the CPU is doubled and the number of cells increases by one-third. These remain high values, notwithstanding the use of wall functions. Also, the maximum CFL number is lower than the subcritical case. It attests to the necessity of wall functions for such high Reynolds numbers.

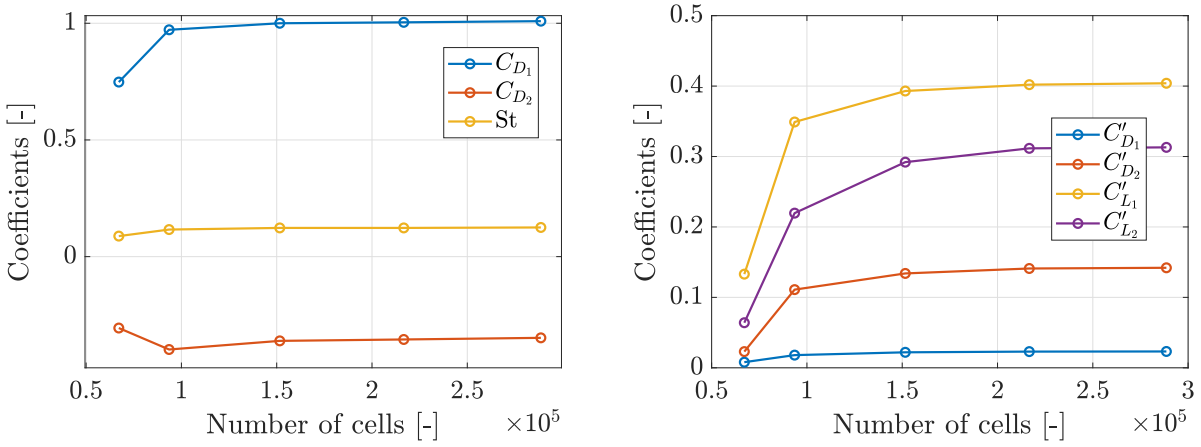

(a) Time-averaged values

(b) Fluctuating values

Figure 3.1: Mesh convergence study of Alam et al. (2003) simulated experiment.

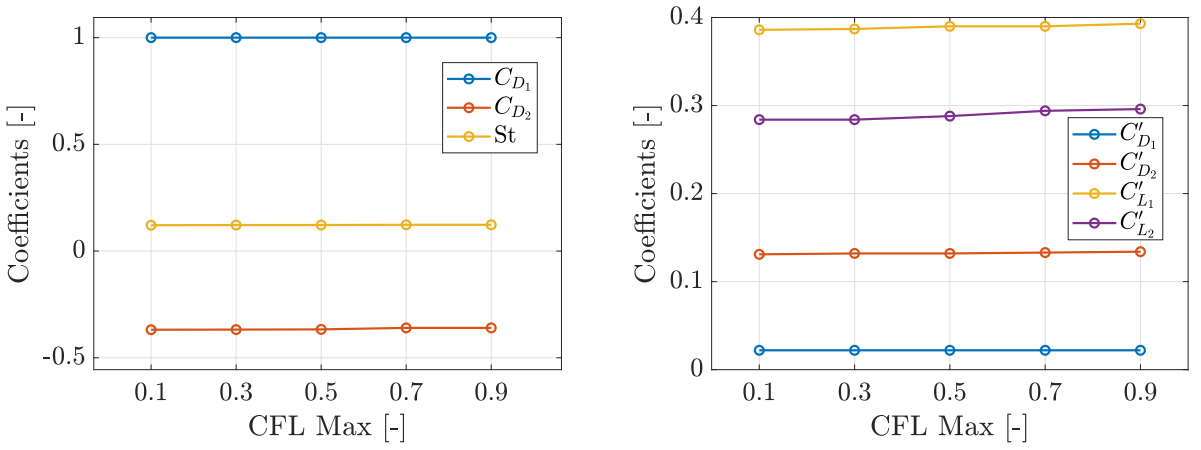

(a) Time-averaged values

(b) Fluctuating values

Figure 3.2: Time convergence study of Alam et al. (2003) simulated experiment.

Parameters	Alam et al. (2003)	Schewe and Jacobs (2019)	Schewe and Jacobs (2019)
Re [-]	6.5×10^4	1.66×10^5	5×10^6
URANS model	$\gamma - \mathrm{Re}_{\theta_t}$	$\gamma - \mathrm{Re}_{\theta_t}$	$k - \omega$ SST
Wall function	no	no	yes
Cells number [-]	1.86×10^5	2.16×10^5	3.18×10^5
CFL max. [-]	0.7	0.5	0.3
CPU [core-hour]	15.1	70	146.7

Table 3.2: Numerical parameters of each simulated experiment.

3.2. Subcritical regime

Simulations around smooth tandem cylinders in the subcritical regime are performed in this section. Table 3.3 summarizes the mean and fluctuating coefficients comparison between the present URANS simulation and the results of Alam et al. (2003). It should be mentioned that all mean lift coefficients are around 10^{-4} and are considered negligible.

The URANS values of the mean coefficients and the Strouhal number are in good agreement with the results of Alam et al. (2003). This is confirmed by the mean pressure distributions comparison in Figure 3.3 (a)-(b). The upstream cylinder coefficients are similar to the single-cylinder ones, except for the Strouhal number, which is much lower for the tandem configuration. For the downstream cylinder, the mean drag is negative. Regarding the fluctuating quantities, higher oscillations for the downstream cylinder drag coefficient than the upstream cylinder. Nevertheless, Alam et al. (2003) also expected higher oscillations for the second cylinder lift coefficient where vortex shedding takes place. In the present URANS case, the first cylinder lift coefficient is slightly higher. In addition, the URANS simulation underestimates the fluctuating pressure, as can be seen in Figure 3.3 (c)-(d). This underestimation in amplitude explains the differences observed with the experimental data for the fluctuating coefficients in Table 3.3.

By analyzing the drag and lift coefficient time histories in Figure 3.4, it can be quickly observed that the drag oscillates twice as fast as the lift, similarly to a single-cylinder described by Sumer and Fredsoe (2006). In this case, it can be attributed to the alternation of the shear layer separation and reattachment. There is quasi zero phase lag between drag and lift coefficients of the same cylinder, but a small phase lag of $\phi(\text{rad}) = 0.15\pi$ can be observed between the two-cylinder lift coefficients. The presence of phase lag is the main difference to the Alam et al. (2003) observations as they reported phase lag only for spacings S/D above 3.

Coeff.	Present URANS	Alam et al. (2003)
Mean		
C_{D_1} [-]	1	1.1
C_{D_2} [-]	-0.36	-0.38
St [-]	0.12	0.12
θ_r [deg]	66.5	66
Fluctuating		
C'_{D_1} [-]	0.02	0.04
C'_{D_2} [-]	0.13	0.19
C'_{L_1} [-]	0.39	0.32
C'_{L_2} [-]	0.3	0.47

Table 3.3: Time-averaged and fluctuating coefficients comparison between the present URANS simulations and Alam et al. (2003).

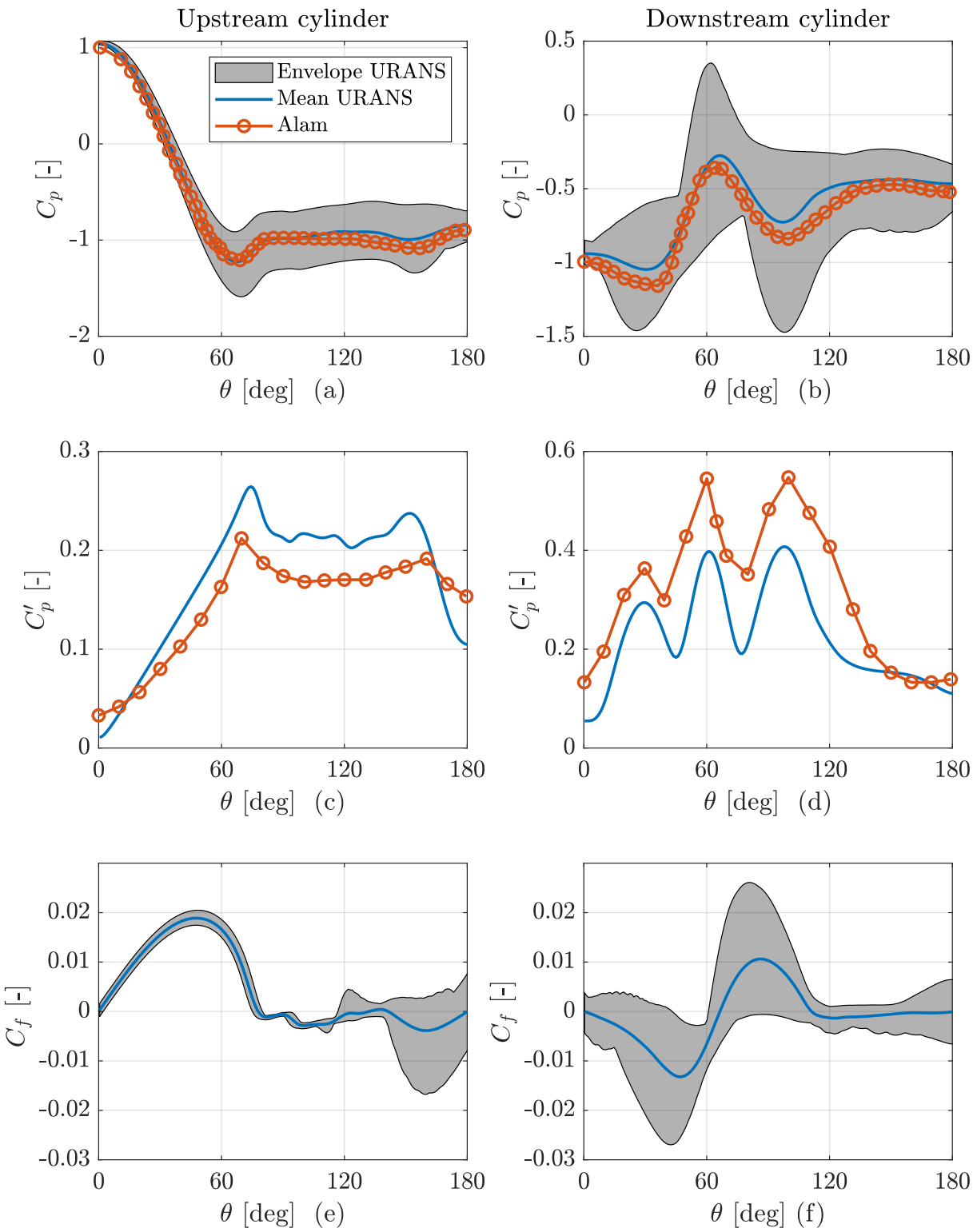

Figure 3.3: Mean and fluctuating pressure and skin friction coefficient distributions over upstream (left) and downstream (right) cylinders. Pressure distributions are compared to Alam et al. (2003).

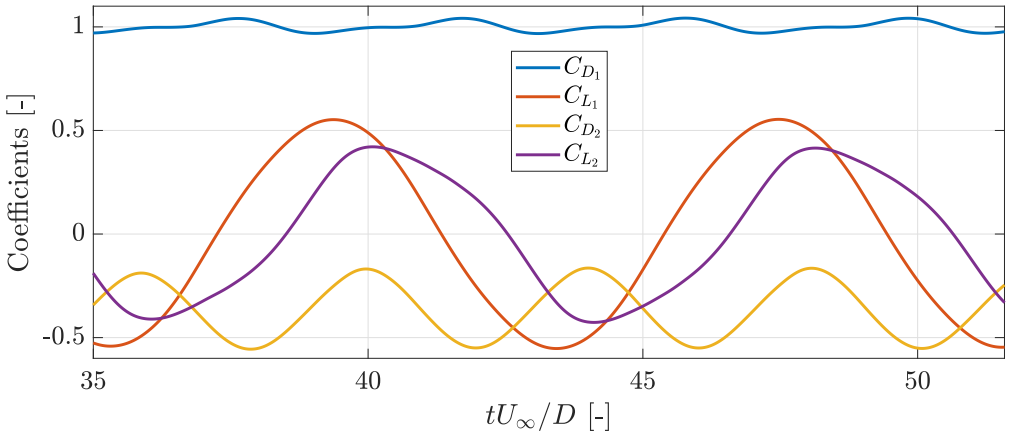

Figure 3.4: Drag and lift coefficient time histories for both cylinders. Alam et al. (2003) experiment is simulated.

Regarding the flow behavior, in Figures 3.3 (e)-(f), the skin friction coefficient distribution presents the separation around 78° for the upstream cylinder, where C_f becomes negative. The flow separation is laminar directly followed by turbulent shear layers in the separated region as confirmed by Figure 3.5. The latter shows the instantaneous contours of intermittency and velocity magnitude near the upstream cylinder separation point. At $\theta = 78°$, i.e., the separation point, the value of γ remains zero, yielding a laminar separation. This effect is the same as for a subcritical flow around a single-cylinder as stated by Achenbach (1968). The shear layers reattach alternately on the downstream cylinder around 66° (angle where C_f becomes positive in Figure 3.3 (f)) and finally separate in a turbulent way around 111° (angle where C_f becomes negative in Figure 3.3 (f)). Alam et al. (2003) observed the same flow separation and reattachment but noticed a second attached zone on the downstream cylinder between 35° and 66°, which finally separates. The present URANS simulations have not captured this latter effect. The envelope of the skin friction coefficient includes all instantaneous distributions. It shows that the upstream cylinder separation point does not fluctuate significantly compared to the downstream reattachment and separation points. In addition, the base pressure of the upstream cylinder is higher than the downstream one due to the different separation behaviors, i.e., turbulent for the downstream cylinder and laminar for the upstream one. The base pressure directly affects the drag coefficients, as explained by Chang (2014) and consequently explains the present differences in drag coefficients for both cylinders.

The flow separation/reattachment can explain the different peaks in the pressure distributions. Indeed, the start of the plateau of the mean upstream cylinder pressure appears around 66°, which is the point where the laminar upstream separation occurs. Less accurate estimation is observed for the separation point by the maximum fluctuating pressure. For the downstream cylinder, the second peak of the mean and fluctuating pressure occurs around 62°, which approximately coincides with the reattachment point. However, the mean pressure gives a more precise estimation of the reattachment point. The downstream separation point, around 112°,

can be approximated when the downstream cylinder plateau in Figure 3.3 (a) begins or by the third peak in the fluctuating pressure in Figure 3.3 (b). It also results in a more precise value thanks to mean pressure information. Alam et al. (2003) expected a more accurate estimation of the reattachment point by the mean pressure than by the fluctuating pressure behavior. In the present case, the same conclusions can be drawn for separation point estimation.

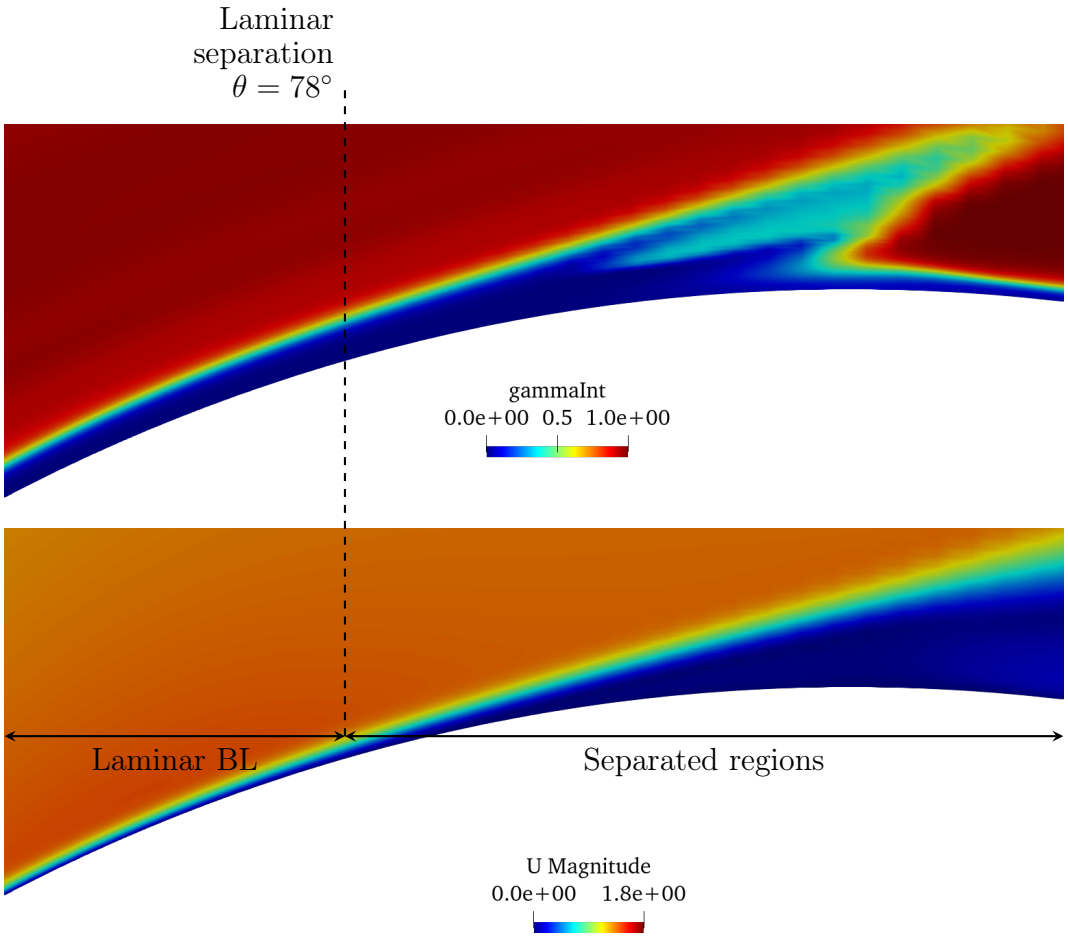

Figure 3.5: Instantaneous intermittency (γ) and velocity magnitude (U) over the top upstream cylinder surface, presenting a laminar separation and turbulent separated regions.

3.3. Subcritical vs. Postcritical

The experiments of Schewe and Jacobs (2019) are simulated for the two Reynolds numbers mentioned in Table 3.1. It allows providing a complete comparison of the Reynolds number impact on the flow around tandem cylinders. Measurements of Jenkins et al. (2006) in the subcritical regime are considered for some distributions when Schewe and Jacobs (2019) do not provide them.

In Table 3.4, mean and fluctuating aerodynamic coefficients are summarized for the two URANS simulations and the two associated experiments of Schewe and Jacobs (2019). Regarding the upstream cylinder mean drag coefficients, URANS simulations underestimate the experimental data but capture the main trend: a higher drag in the subcritical than in the postcritical regime. As for a single-cylinder described by Achenbach (1968), the BL is laminar on the upstream cylinder when separation occurs in the subcritical regime, while it is turbulent in the postcritical regime. This different nature of BLs has two main consequences. First, the turbulent BL, associated with postcritical flow, separates at a higher angle than a laminar boundary layer. This difference in angle of separation can be seen in Figure 3.6 (e) when C_f becomes zero at 77° for subcritical and at 102° for postcritical. It leads to a narrower wake for the postcritical regime and a decrease in the drag coefficient. Secondly, the base pressure in Figure 3.6 (a) for the subcritical flow is lower than the postcritical one. The lower base pressure tends to increase the drag coefficients.

Regarding the mean drag coefficient of the downstream cylinder, URANS simulations are in good agreement with all Schewe and Jacobs (2019) data. Indeed, as expected by Schewe and Jacobs (2019), the drag coefficient of the downstream cylinder increases when going from subcritical to postcritical flow regime but remains negative. The differences between the two drag coefficients are due to the different reattachment points on the downstream cylinder. As the upstream wake is narrower for the postcritical regime, the flow reattaches at a lower angular position. As the flow is longer separated for the subcritical regime, a stronger recirculation region is created for this regime, yielding a lower drag coefficient. This different reattachment angular position can be observed in Figure 3.6 (f), where C_f becomes positive around 56° for the postcritical regime and around 68° for the subcritical one. Both BLs are turbulent on the downstream cylinder, and a BL associated with the postcritical regime is less sensitive to separation compared to the BL in a subcritical regime as described by Schlichting and Gersten (1979). However, separations occur at a similar point for both regimes as the postcritical BL reattaches at a smaller angle. The separations can be seen in Figure 3.6 (f) where C_f becomes negative around 112°. This similarity in separation between the two regimes leads to the same base pressure in Figure 3.6 (b). Finally, for both cylinders, the postcritical skin friction coefficient is much lower than the subcritical one. This is a direct consequence of the difference in Reynolds number (ratio of inertia to viscous forces).

The fluctuating coefficients, which are not provided by Schewe and Jacobs (2019), globally indicate that the amplitude of the lift and drag coefficients are weaker for the postcritical than the subcritical regimes, as noticed by numerical the simulations of Hu et al. (2019) and Dubois and Andrianne (2021) for their experiments on the flow around rough cylinders. The narrower wake for the postcritical regime, highlighted by the lower total drag coefficient in Table 3.4, can explain this decrease in coefficients. Figures 3.6 (c)-(d) present the fluctuating pressure coefficient where the same effects are visible, i.e., lower fluctuations in the postcritical regime. The peaks in fluctuating pressure for the upstream cylinder are shifted due to the differences in the separation angles. For the downstream cylinder, the peaks appear simultaneously as the separation angle is the same. Furthermore, the minimum mean pressure in Figure 3.6 (a) and the rear plateau in Figure 3.6 (b) approximately appear when separations occur. These are two ways to detect separation if the skin friction coefficient cannot be extracted. However, as already mentioned, Alam et al. (2003) expected more accurate estimations when the mean pressure coefficients are analyzed.

Compared to the distribution of Jenkins et al. (2006) in Figure 3.6 (a), the mean pressure of the upstream cylinder presents significant differences around 70° in amplitudes, but the peaks appear for the same angles, and the base pressure is correctly estimated. Regarding the downstream cylinder, high differences in pressure magnitude appear around 30° and 90° but the entire behavior and the base pressure are correctly approximated.

Coeff.	URANS	URANS	Schewe and Jacobs (2019)	Schewe and Jacobs (2019)
Re [-]	1.66×10^5	5×10^6	1.66×10^5	5×10^6
Mean				
C_{D_1} [-]	0.73	0.4	1	0.47
C_{D_2} [-]	-0.36	-0.076	-0.37	-0.072
$C_{D_{1+2}}$ [-]	0.37	0.32	0.63	0.4
St [-]	0.28	0.3	-	-
Fluctuating				
C'_{D_1} [-]	0.005	0.0005	-	-
C'_{D_2} [-]	0.004	0.0005	-	-
C'_{L_1} [-]	0.02	0.001	-	-
C'_{L_2} [-]	0.05	0.023	-	-

Table 3.4: Time-averaged and fluctuating coefficients at two Reynolds numbers for the present URANS and Schewe and Jacobs (2019) experiments.

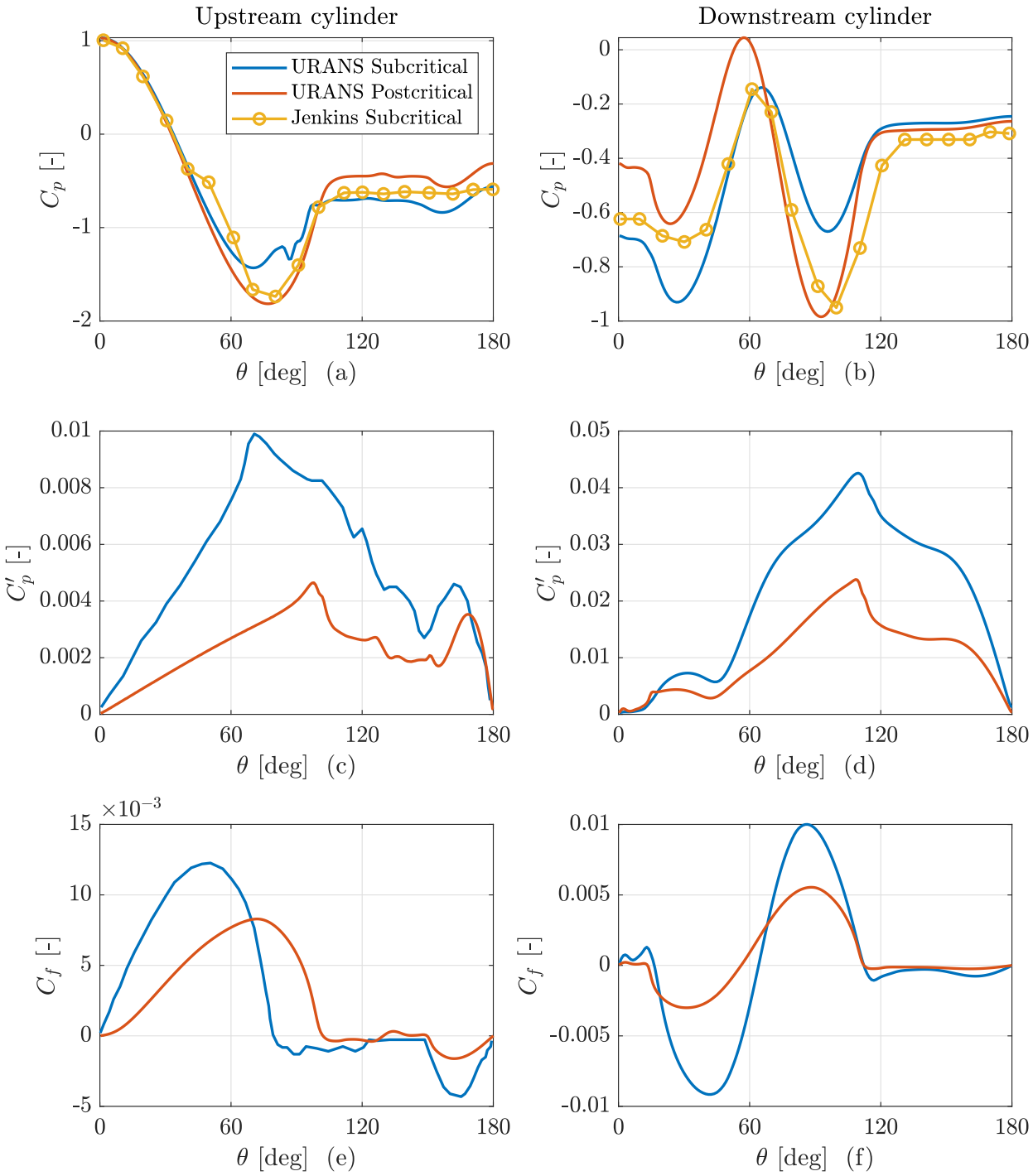

Figure 3.6: Mean and fluctuating pressure distributions and skin friction coefficient for both flow regimes. Mean pressure distributions of Jenkins et al. (2006) are introduced for the subcritical regime.

Figure 3.7 and 3.8 analyze the impact of the flow regime on mean streamwise and vertical velocities and the turbulent kinetic energy in the wake of the downstream cylinder. These comparisons have been widely used: Garbaruk et al. (2010), Uzun and Hussaini (2012), Gopalan and Jaiman (2015) and Hu et al. (2019), and allow characterizing the flow behavior in the wake (recirculation length, dissipation of turbulent kinetic energy, momentum deficit). Jenkins et al. (2006) data for mean TKE and streamwise velocity along the centerline are introduced for subcritical comparison in the downstream cylinder wake. Some authors also present the profiles between the two cylinders. However, as the gap is relatively small in the present case, it has no interest to present these comparisons. Indeed, no vortex shedding takes place behind the upstream cylinder.

First, the non-dimensionalized streamwise velocity tends to converge more quickly through the freestream velocity in the postcritical regime. After that, the recirculating length can be estimated to $L_r/D = 1.1$ for both regimes from Figure 3.7 (a) (the zone where the mean streamwise velocity is negative on the centerline). For a single-cylinder, recirculation lengths are not in both regimes the same as the separation points are different. However, in the present case, as the downstream cylinder separation angle is quasi the same, the same wake behavior can be expected for a tandem cylinder in both regime. By comparing the recirculation length results to Jenkins et al. (2006), it can be seen that URANS simulations overestimate this quantity as experimental results lie around $L_r/D = 0.7$. This discrepancy highlights URANS limitations in capturing the wake topology of bluff bodies. DES of Travin et al. (2000) and LES of Breuer (1999) also overestimated the numerical estimation of recirculation length for a single-cylinder. None of them could report a precise reason for these discrepancies. The TKE distributions along the centerline in the downstream cylinder wake in Figure 3.7 (b) are pretty similar for both regimes. Higher values in the profile can be observed for the subcritical regime. In the postcritical regime, the TKE decay is stronger than in the subcritical regime. The latter profile is in good agreement with the measurements of Jenkins et al. (2006).

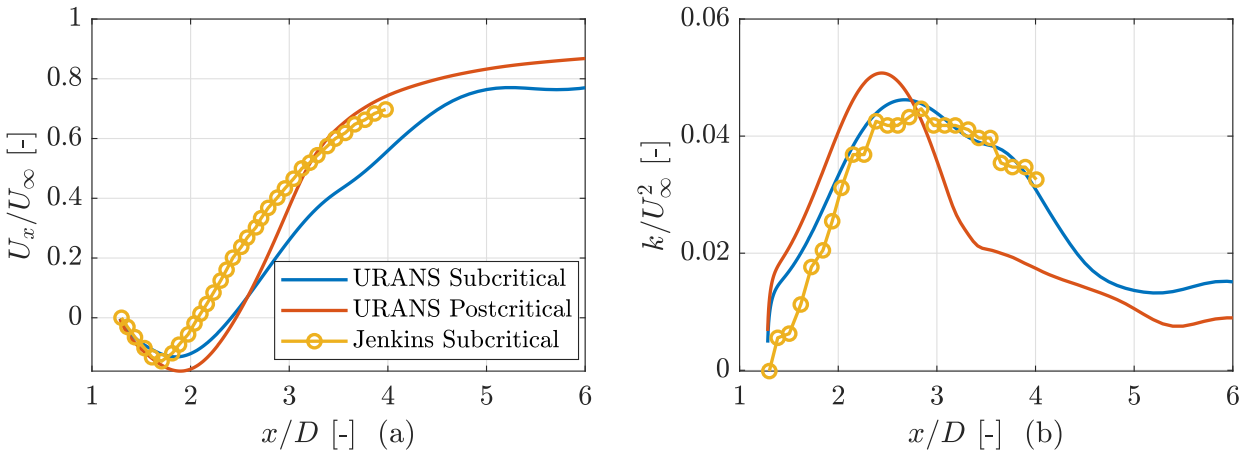

Figure 3.7: Mean streamwise velocity and mean turbulent kinetic energy (k) along the centerline in the downstream cylinder wake for both regimes. Distributions of Jenkins et al. (2006) are introduced for the subcritical regime.

For the vertical and streamwise velocity profiles, two different cases are considered: one profile inside the recirculation region ($x/D = 1.78$ in Figures 3.8 (a)-(b)) and the second one outside ($x/D = 3.78$ in Figures 3.8 (c)-(d)). Inside the recirculation region, small differences appear between both regimes. As $x/D = 1.78$ is inside the recirculation region, a small negative mean streamwise velocity appears along the centerline ($y/D = 0$) in Figure 3.8 (a). For vertical velocity, an anti-symmetric profile is presented in Figure 3.8 (b) and also highlights small differences between the two regimes.

Higher differences appear outside the recirculation region. In Figure 3.8 (c), the deficit in mean streamwise velocity is slightly higher for the subcritical regime outside the recirculation region on the centerline ($y/D = 0$). Here, the mean streamwise velocity at the centerline is positive, confirming that $x/D = 3.78$ is outside the recirculation region. This figure gives an idea of the total tandem drag, which is higher for subcritical case (*cfr.* Table 3.4). In Figure 3.8, the subcritical regime presents a higher vertical velocity profile, leading to a narrower wake for the postcritical regime as expected by previous discussions. In this figure, U_y presents an anti-symmetric profile and only experiences one change of sign, while inside the recirculation region, three changes of sign were observed.

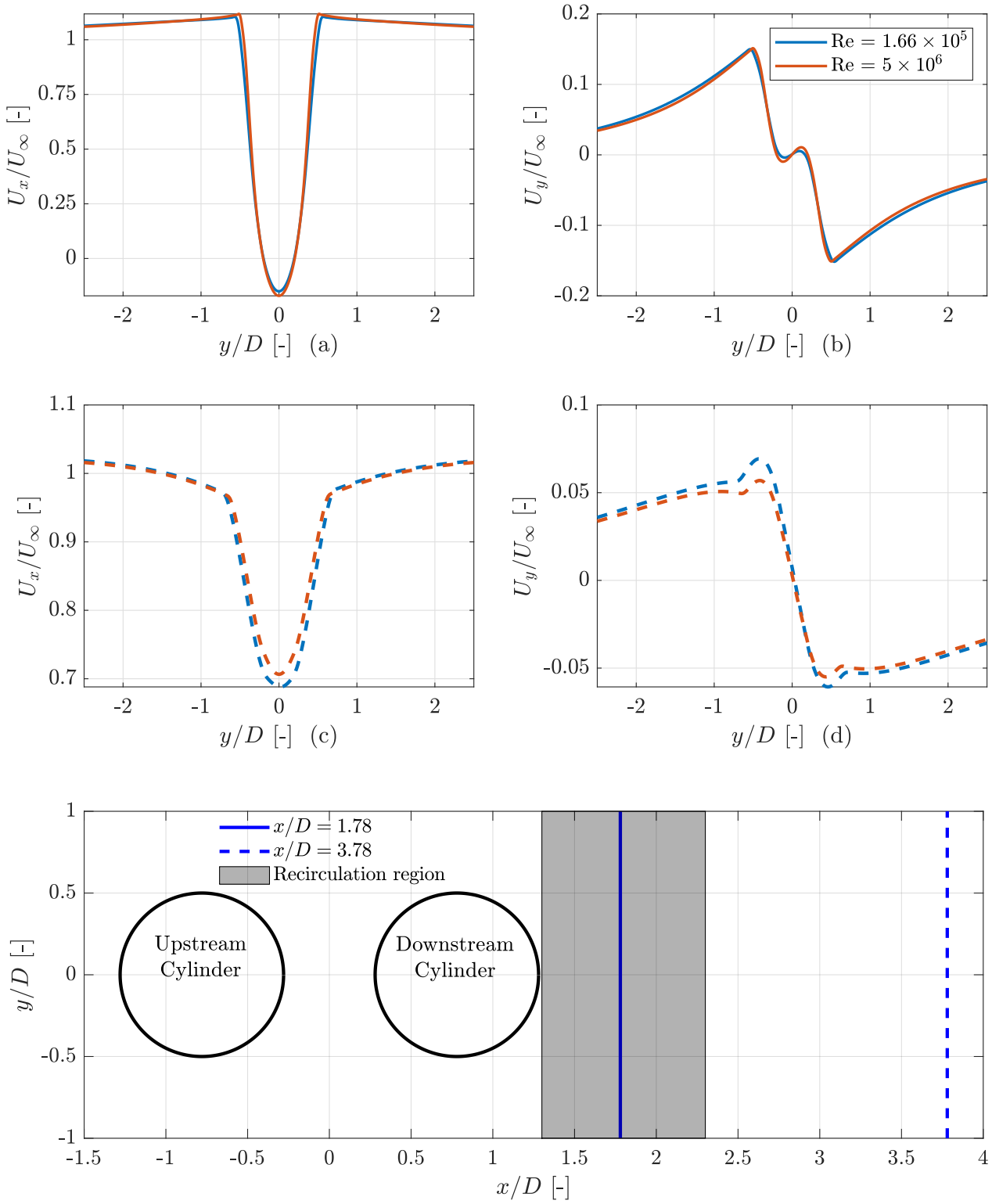

Figure 3.8: Mean streamwise and vertical velocities profiles in the downstream cylinder wake. $x/D = 1.78$ (upper Figures) and $x/D = 3.78$ (lower Figures).

4. Results

This section covers the results and discussions associated with Reynolds number and roughness effects for the tandem cylinders. The models have been validated for smooth tandem cylinders in the subcritical and postcritical regimes. The effects of Reynolds in the subcritical regime are first studied. Indeed, differences in Strouhal and in fluctuating aerodynamic forces appear between the experiments of Jenkins et al. (2006) and Alam et al. (2003). The latter considered two Reynolds numbers in the subcritical regime. The Reynolds effects are not studied in the postcritical regime as much fewer changes are expected than for the subcritical regime and as computational resources are limited. After that, rough tandem cylinders are analyzed, and results are compared to experimental results of Dubois and Andrianne (2021). Comparisons of the aerodynamic coefficients, flow and wake analyses are performed. Finally, flow topologies of smooth and rough tandem cylinders in the subcritical and postcritical regimes are compared.

4.1. Smooth cylinders

This section focuses on the effects induced by the Reynolds number in the subcritical regime. To do so, the spacing $S/D = 1.56$ and turbulence intensity $Tu = 0.4$ % of Schewe and Jacobs (2019) are considered while the range of Reynolds goes from 4.5×10^4 to 2×10^5. The present results are compared to the data of Schewe and Jacobs (2019) when available. Figure 4.1 presents the overall Reynolds effects on the mean and fluctuating aerodynamic coefficients, the Strouhal number, the separation and reattachment angles and the base pressure coefficient.

The Strouhal number switches from 0.12 to 0.28 between Re $= 1.33 \times 10^5$ and 1.4×10^5, in Figure 4.1 (a). Globally, the downstream cylinder experienced higher fluctuation in its aerodynamic coefficients as vortex shedding only occurs for the downstream cylinder. Also, around Re $= 1.4 \times 10^5$, a drop of fluctuating aerodynamic coefficients can be observed in Figure 4.1 (b). In addition, the drag coefficient of the upstream cylinder significantly decreases between Re $= 1.66 \times 10^5$ and 2×10^5. Therefore, throughout this Reynolds analysis, some velocity and intermittency contours and velocity and TKE profiles are presented for three Reynolds numbers (1.33×10^5, 1.66×10^5, and 2×10^5). These Reynolds numbers allow considering all changes induced by Strouhal switch, drag crisis, and drop of fluctuations.

In Figure 4.1 (a), the upstream cylinder has similarities with a single-cylinder, i.e., its drag coefficient decreases with the Reynolds number due to the delay in the separation in Figure 4.1 (c). Figure 4.2 shows the instantaneous contours of the magnitude of U for three Reynolds numbers. A larger upstream cylinder wake can be observed for Re $= 1.33 \times 10^5$ and 1.66×10^5 while for Re $= 2 \times 10^5$, this wake is extremely reduced as confirmed by the value of $C_{D_1} = 0.41$ in Figure 4.1. This delay also affects the base pressure, which tends to increase in Figure 4.1 (d). The separation is laminar for the three Reynolds numbers as highlighted by Figure 4.3,

where the quantity γ remains zero until separation. Drag crisis, expected by Schewe and Jacobs (2019) to take place around $\mathrm{Re} = 3 \times 10^5$, seems to occur around 2×10^5 in the present simulations. This critical Reynolds number underestimation can be seen in Figure 4.1 (a), where the upstream mean drag coefficient of Schewe and Jacobs (2019) is much higher than the one of the present URANS.

Regarding the downstream cylinder, its mean drag coefficient increases with the Reynolds number and becomes quasi zero around $\mathrm{Re} = 2 \times 10^5$. This phenomenon shows that the mean drag coefficient of both cylinders behaves conversely. The flow reattachment occurs sooner on the downstream cylinder when the Reynolds number increases, as shown in Figure 4.1 (c). This lower angle of reattachment is caused by the delay in the upstream cylinder and the associated narrower wake. Finally, the downstream separation angle does not evolve a lot for two main reasons. Firstly, the upstream cylinder boundary layer is turbulent, and secondly, the Reynolds change cannot affect the flow behavior to an adverse pressure gradient. Consequently, the base pressure of the downstream cylinder does not evolve as the upstream one.

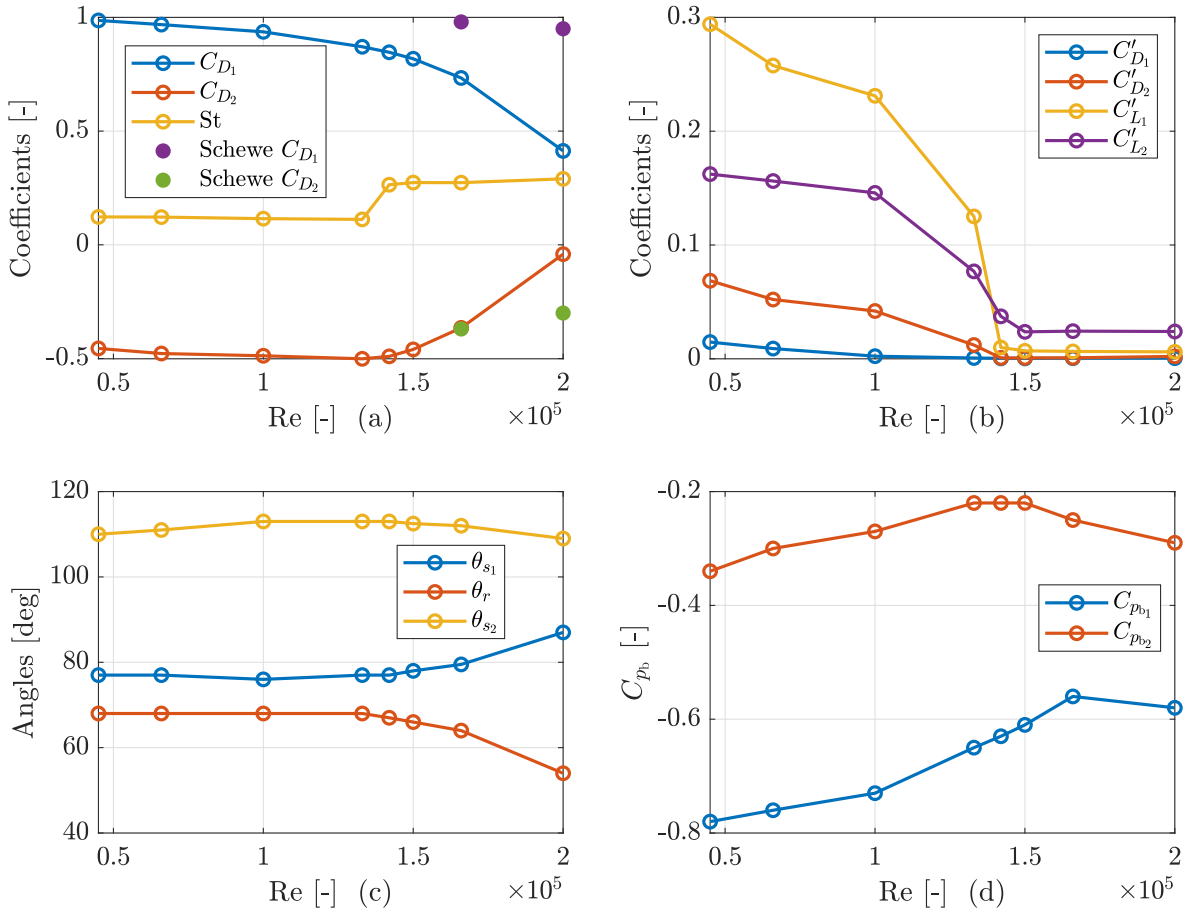

Figure 4.1: Reynolds effect in the subcritical regime for aerodynamic coefficients [-], separation and reattachment angles [deg], and base pressure coefficients [-].

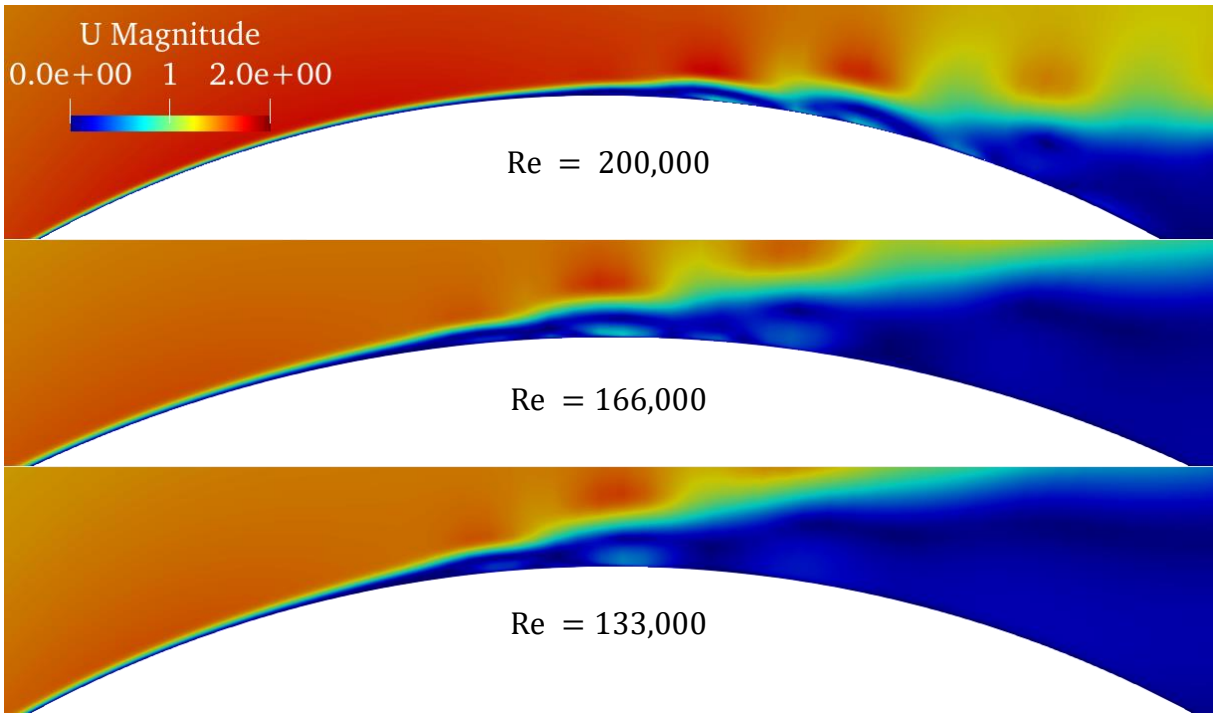

Figure 4.2: Instantaneous U magnitude contours on the top of the upstream cylinder surface for three subcritical Reynolds numbers.

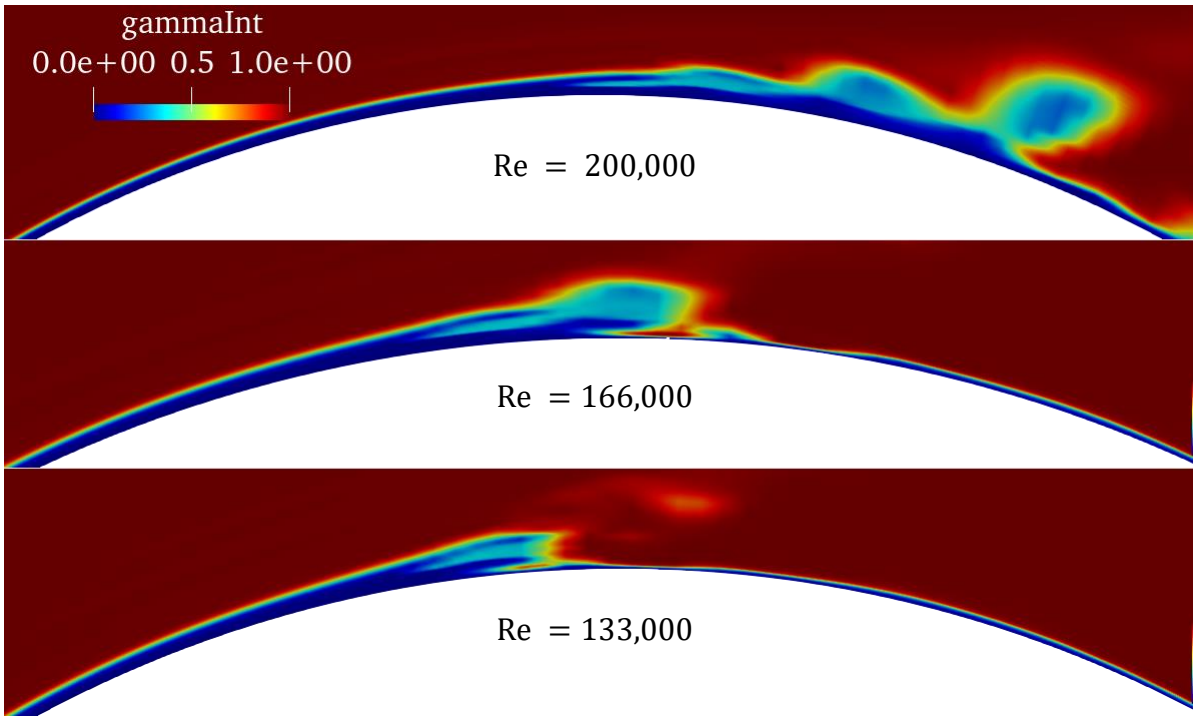

Figure 4.3: Instantaneous γ contours on the top of the upstream cylinder surface for three subcritical Reynolds numbers.

To conclude this Reynolds number effect study, TKE and velocity profiles are plotted in the downstream cylinder wake. As in Section 3.3, the profiles are not plotted between the two cylinders. Indeed the gap is quite small and no vortex shedding takes place. First of all, it should be mentioned that the overall tandem drag ($C_{D_1} + C_{D_2}$) is around 0.41, 0.36 and 0.37 for Re $= 1.33 \times 10^5$, 1.66×10^5 and 2×10^5, respectively. Figure 4.4 presents the TKE and mean streamwise velocity along the centerline. The recirculation region length is the same for Re $= 1.33 \times 10^5$ and 1.66×10^5 and is slightly higher for Re $= 2 \times 10^5$, as can be seen in Figure 4.4 (a). The streamwise velocity tends more quickly through U_∞ for Re $= 1.66 \times 10^5$ and Re $= 2 \times 10^5$ as their total drag coefficient is similar and lower than at Re $= 1.33 \times 10^5$. The same effects are observed for TKE distributions in Figure 4.4 (b), whose decay is higher for Re $= 1.66 \times 10^5$ and 2×10^5. As different behaviors are observed inside and outside the recirculation region, the two regions are considered for streamwise and vertical velocity comparison along the vertical coordinate (y/D). In Figure 4.5 (a), inside the recirculation region, all profiles are very similar. A negative streamwise velocity is found at the centerline for all Reynolds numbers, confirming that $x/D = 1.78$ is inside the recirculation region. Figure 4.5 (b) presents small differences between the Reynolds numbers, with three changes of sign for U_y. Larger differences can be observed outside the recirculation region. In Figure 4.5 (c), the streamwise velocity profiles give an idea of the total tandem drag coefficients. As expected, the highest deficit is observed for Re $= 1.33 \times 10^5$, and the lowest one appears for Re $= 1.66 \times 10^5$. U_x is positive for every value of y/D, confirming that $x/D = 3.78$ is outside the recirculation region. Finally, in Figure 4.5 (d), the vertical velocity profile associated with Re $= 1.33 \times 10^5$ presents the highest deficit while the one associated with Re $= 1.66 \times 10^5$ presents the lowest. Outside the recirculation region, only one change of sign is experienced.

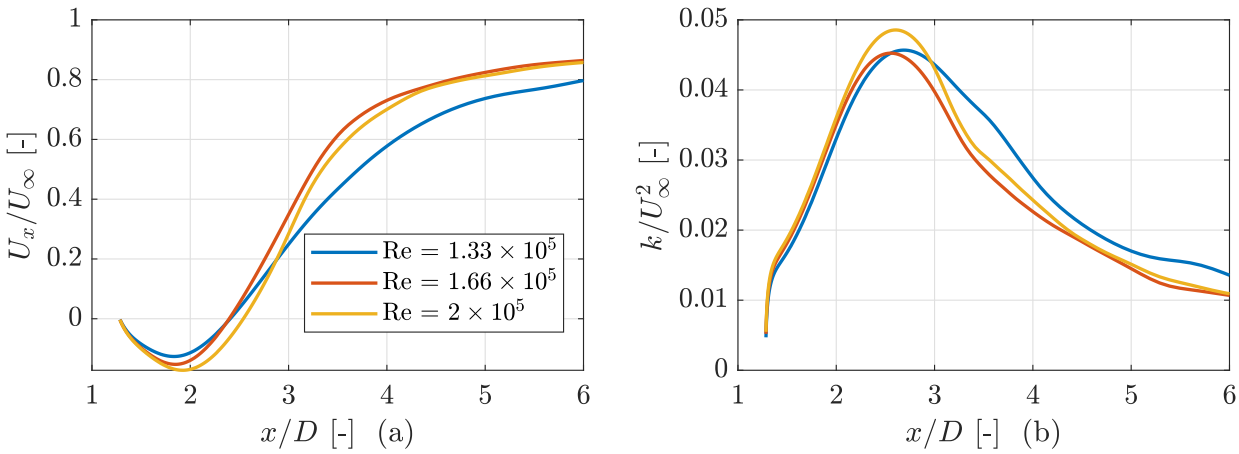

Figure 4.4: Comparison of the mean streamwise velocity (U_x) and mean turbulent kinetic energy (k) along the centerline in the downstream cylinder wake for three subcritical Reynolds numbers.

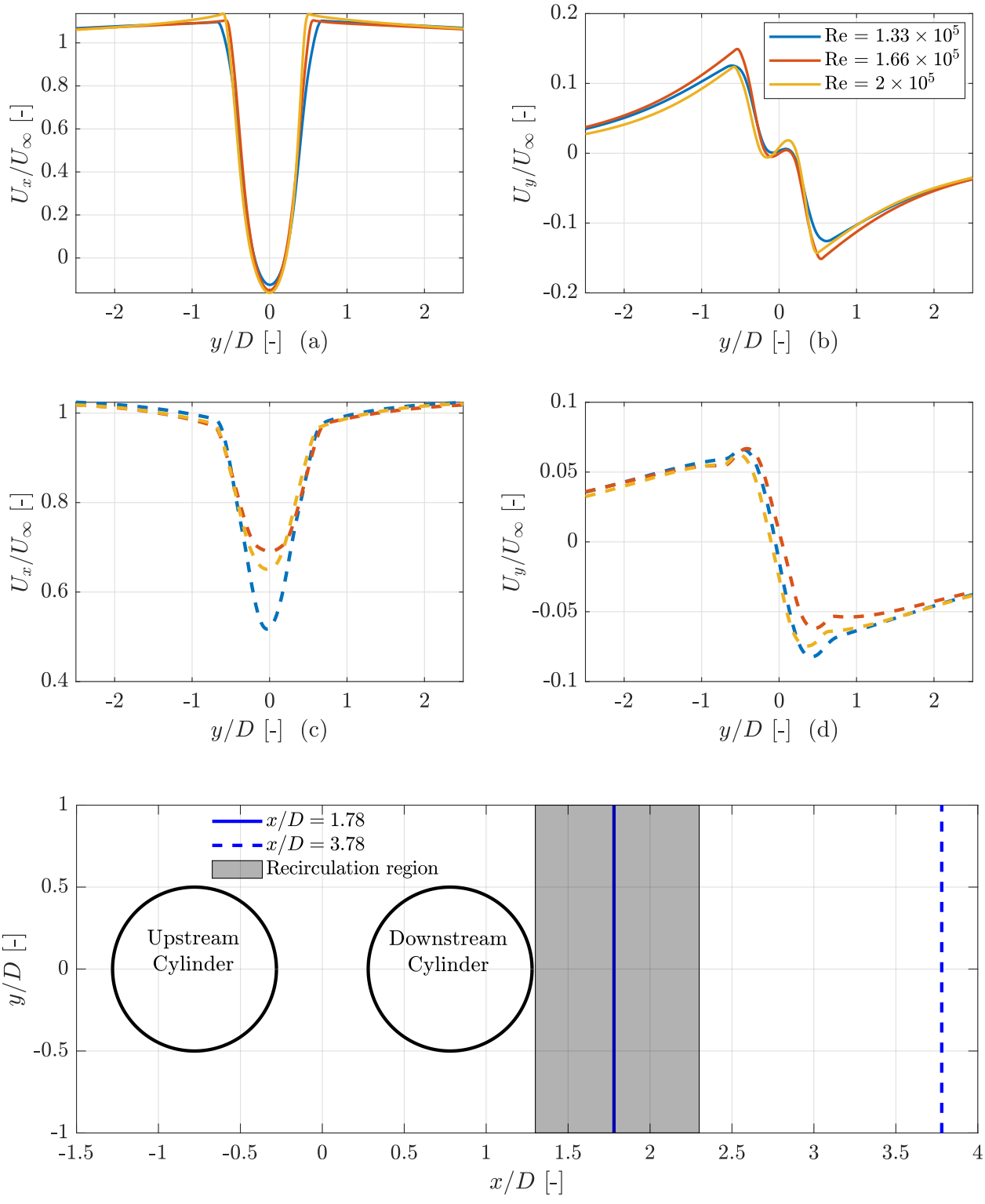

Figure 4.5: Comparison of the mean streamwise and vertical velocities profiles in the downstream cylinder wake for three subcritical Reynolds numbers. $x/D = 1.78$ (solid line) and $x/D = 3.78$ (dotted line).

4.2. Rough cylinders

In this section, URANS simulations are performed on rough tandem cylinders. The same solvers, BCs, computational domain, and numerical parameters of Section 2.2 are considered. The adaptive time step is considered, and the previously used meshes are adapted in the radial direction to meet y^+ wall function requirements. To model roughness, complex methods exist, such as modeling roughness elements by closely spaced ellipsoids. Rodríguez et al. (2016) used this method for its LES simulations, but it requires complex meshing near the wall in the BL. It is not the goal of the present research. To make it simpler, as explained in Section 2.2, wall functions can be employed to model roughness. However, as pointed by Liu and Qin (2015), the transition model ($\gamma - \mathrm{Re}_{\theta_t}$) cannot deal with rough and smooth wall functions. Therefore, only the classical $k-\omega$ SST model will be employed when dealing with rough cylinders. In the subcritical regime, notwithstanding very high roughness values, the laminar-to-turbulent transition has an impact on flow behavior and aerodynamic forces as described by Achenbach (1971). For higher Reynolds numbers, the roughness triggers the laminar-to-turbulent transition well before separation as explained by Rodríguez et al. (2016). Therefore, in the postcritical regime, the transition has even less impact than in the smooth case. In the following, the results associated with the subcritical flow with rough cylinders must be considered with prudence. Indeed, even for a smooth single case in Section 2.3, wall functions yield very bad approximations as no transition modeling can be employed. However, wall functions provided very satisfying results in the postcritical regime around a single-cylinder and tandem cylinders, as shown by comparison in Sections 2.3 and 3.3.

In this section, the experiments of Dubois and Andrianne (2021) are taken as references. Two Reynolds numbers are considered: $\mathrm{Re} = 4.5\times10^4$ and 3.95×10^5. The spacing S/D is the same as Schewe and Jacobs (2019), i.e., 1.56 and the roughness is uniform and its non-dimensional height is $K_s/D = 7.2\times10^{-3}$. With this level of roughness, Dubois and Andrianne (2021) assume a subcritical flow regime at $\mathrm{Re} = 4.5\times10^4$ and a postcritical one at $\mathrm{Re} = 3.95\times10^5$. Finally, the turbulence intensity of the incoming flow is at 0.2 %. The pressure distributions of Dubois and Andrianne (2021) are extracted every 7.5°, limiting the precision in estimating characteristic points. Table 4.1 summarizes main numerical parameters of the simulated experiments of Dubois and Andrianne (2021). As it can be seen, notwithstanding the use of wall functions, much higher CPU resources are required for the higher Reynolds number as more cells are required in the BLs. Also, the maximum CFL number is higher for the lower Reynolds number case. Regarding the post-processing of the results, as previously done, aerodynamic coefficients, pressure distributions, skin friction coefficient distributions, and velocity profiles are analyzed to assess URANS validity and are used to compare the main effects induced by roughness at two different Reynolds numbers.

Parameters	Dubois and Andrianne (2021)	Dubois and Andrianne (2021)
Re [-]	4.5×10^4	3.95×10^5
URANS model	$k-\omega$ SST	$k-\omega$ SST
Wall function	yes	yes
Cells number [-]	4×10^4	1.86×10^5
CFL max. [-]	0.7	0.5
CPU [core-hour]	1.4	30.2

Table 4.1: Numerical parameters of rough tandem cylinders simulations.

4.2.1. Aerodynamic forces and Strouhal number

Table 4.2 summarizes the mean pressure drag coefficient, the Strouhal number, and the friction percentage for both simulated experiments. This table also includes their associated experimental results. As the experimental data do not provide skin friction results, the drag has been computed by integrating the pressure coefficient along the cylinder surface, leading to C_{D_p}. The same integration is performed for URANS data. From experimental results, it can be concluded that the upstream drag coefficient decreases in the postcritical regime compared to the subcritical one but remains high compared to smooth cylinder results (*cfr.* Table 3.4 in Section 3.3). URANS simulations give high drag coefficients for both regimes but miss the trend as they provide a higher drag for the subcritical than the postcritical regime.

Regarding the downstream drag coefficient, the experimental data shows that, for both regimes, the drag coefficient is negative with a higher value in the postcritical regime. URANS simulations capture this trend but overestimate both drag coefficients for the downstream cylinder. As a consequence of the previous discrepancies, especially for the upstream cylinder, the URANS value of the total drag coefficient ($C_{D_{1+2}}$) is higher in the postcritical regime than in the subcritical regime, which is a contradiction with Dubois and Andrianne (2021) experimental results. Regarding the Strouhal number, Dubois and Andrianne (2021) reported a bi-stable behavior for the postcritical regime, giving two Strouhal number values. URANS simulations cannot capture that phenomenon but give acceptable approximations for both regimes. By analyzing Table 3.4 in Section 3.3, meaningful changes are observed in the Strouhal number between smooth and rough cylinders for both regimes. It results that frequency of the vortex shedding pattern behind the downstream cylinder is reduced by roughness. Finally, friction drag can be computed for URANS results. The friction percentage at $\mathrm{Re} = 3.95 \times 10^5$ for the upstream cylinder is in good agreement with the 2.5 % of Achenbach (1971), whose experiment con-

cerned a rough single-cylinder with similar characteristics. However, the friction percentage at $\mathrm{Re} = 4.5 \times 10^4$ for the upstream cylinder does not approximate correctly the value observed by Achenbach (1971), i.e., 0.5 %.

Coeff.	URANS	URANS	Dubois and Andrianne (2021)	Dubois and Andrianne (2021)
Re [-]	4.5×10^4	3.95×10^5	4.5×10^4	3.95×10^5
St [-]	0.13	0.13	0.15	0.15-0.23
Pressure				
$C_{D_{p,1}}$ [-]	0.91	0.94	1.18	1.01
$C_{D_{p,2}}$ [-]	-0.46	-0.34	-0.5	-0.39
$C_{D_{p,1+2}}$ [-]	0.45	0.6	0.68	0.62
Friction				
$C_{D_{f,1}}/C_{D_1}$ [%]	3.2	3.1	-	-
$C_{D_{f,2}}/C_{D_2}$ [%]	6.12	2.9	-	-

Table 4.2: Pressure drag, friction drag percentage and Strouhal number comparison for the present URANS and experiments of Dubois and Andrianne (2021).

4.2.2. Pressure distribution

Figures 4.6 and 4.7 show the mean pressure, fluctuating pressure, and skin friction coefficient distribution over both cylinders for subcritical and postcritical regimes, respectively. The envelopes of the mean pressure and skin friction coefficients, corresponding to regions including all results, are also plotted in light gray. As previously done in the smooth case (*cfr.* Figures 3.3 and 3.6 in Section 3.3), the different curves allow analyzing the flow behavior and assessing more precisely the validity of the URANS simulations.

Regarding the mean pressure distribution in the subcritical regime in Figures 4.6 (a)-(b), the URANS results are in good agreement concerning the curve behavior. Indeed, the peaks are reached at the same angles as the experimental results for both cylinders. However, some differences are present in pressure amplitude, i.e., the URANS simulations provide lower pressure values, especially for the base pressure, leading to higher drag coefficients in Table 4.2. In the postcritical regime, in Figures 4.7 (a)-(b), the URANS results are in better agreement with the experimental results regarding the amplitudes. There is still a small discrepancy in pressure amplitudes resulting in a small overestimation for the drag coefficients in Table 4.2. The peaks are well approximated but a shift is observed around $\theta = 65°$ in Figure 4.7 (b).

The fluctuating pressure distributions on the downstream cylinder computed by URANS simulations in Figure 4.6 (d) are in good agreement regarding the experimental results. The peaks are well approximated, but the pressure fluctuations are underestimated by the URANS model, leading to lower fluctuating drag and lift coefficients. Regarding the upstream cylinder distribution in 4.6, divergences appear compared to experimental data. The first peak is correctly approximated but slightly shifted while the rear fluctuating pressure does not behave as the experimental one. This observed behavior is different from other experiments. Indeed, for example, in the Alam et al. (2003) experiment, the fluctuating pressure of the upstream cylinder decreased at the rear. This new behavior can be attributed to roughness, leading to increased pressure fluctuations in the upstream cylinder wake. However, as for smooth tandem cylinders, fluctuations remain higher for the downstream cylinder, as the vortex shedding phenomenon can fully develop behind the latter. Globally, by referring to Alam et al. (2003) results, pressure fluctuations are weaker for a rough tandem cylinder than a smooth one.

Concerning the postcritical regime, Figure 4.7 (c) shows differences between experimental and URANS results for the upstream cylinder. In addition to the pressure fluctuations overestimation, the fluctuating pressure at the rear is not captured by URANS simulations. URANS expect a decrease of the fluctuations while experiments not. Regarding the downstream cylinder fluctuating pressure in Figure 4.7 (d), the amplitude is in good agreement, but fluctuation behaviors are different. Discrepancies appear as URANS simulations expect three peaks around 30°, 60°, and 100° while experimental results only present one peak at 70°. As for the subcritical regime, higher pressure fluctuations are observed for the downstream cylinder. Finally, while Dubois and Andrianne (2021) expect lower pressure fluctuations in the postcritical regime than in the subcritical for both cylinders and especially the upstream one, URANS simulations provide the same order of magnitude for both regimes.

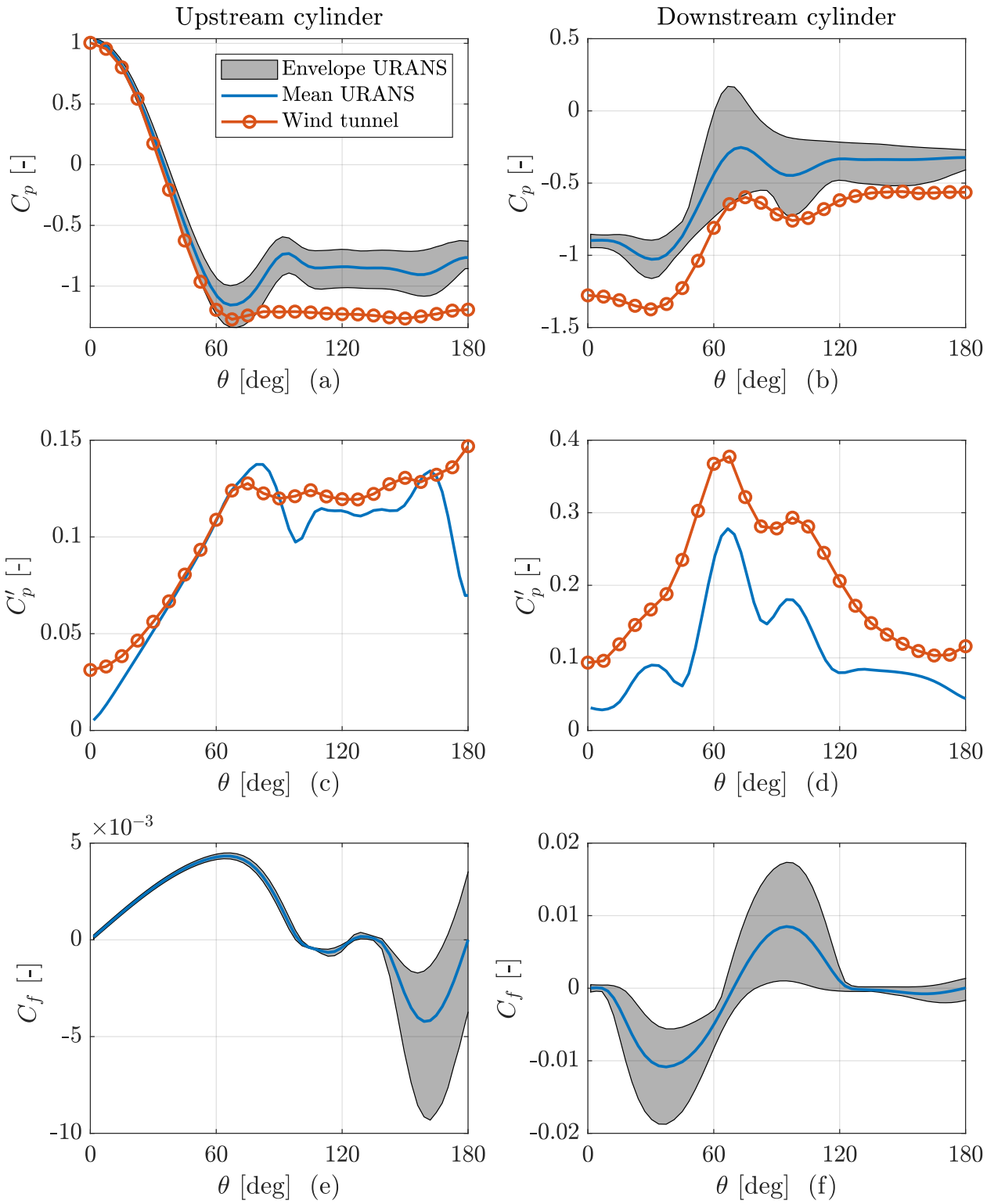

Figure 4.6: Mean and fluctuating pressure and skin friction coefficients distribution over the two cylinders at $\mathrm{Re} = 4.5 \times 10^4$. Envelopes of mean pressure and skin friction coefficient are also plotted. Wind tunnel data from Dubois and Andrianne (2021) are introduced for comparison.

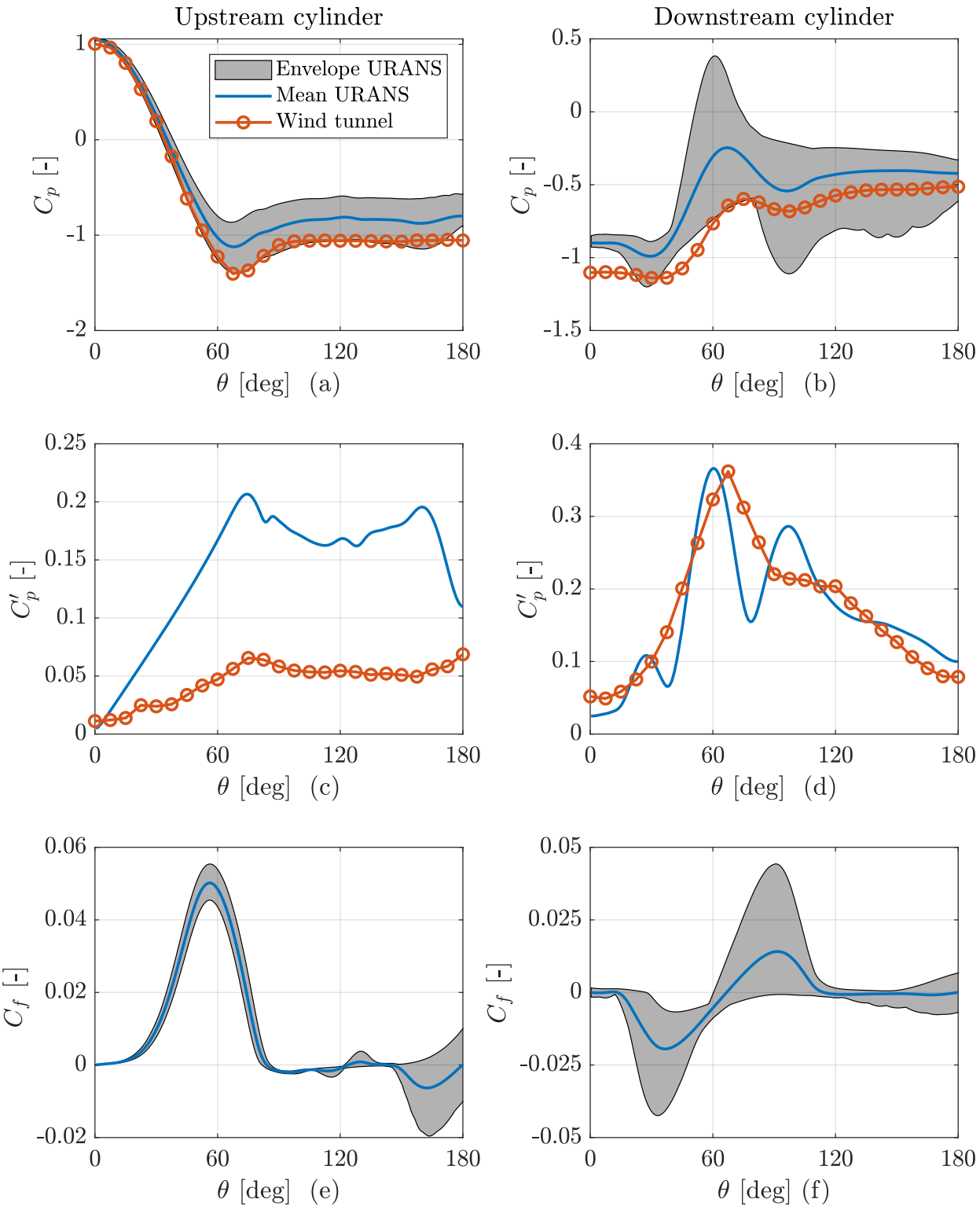

Figure 4.7: Mean and fluctuating pressure and skin friction coefficients distribution over the two cylinders at Re = 3.95×10^5. Envelopes of mean pressure and skin friction coefficient are also plotted. Wind tunnel data from Dubois and Andrianne (2021) are introduced for comparison.

4.2.3. Flow analysis

Separation/Reattachment points

Separation and reattachment points for both cylinders in both flow regimes can be extracted for URANS simulations through the to skin friction behavior in Figures 4.6 (e)-(f) and 4.7 (e)-(f). As experimental results do not give access to skin friction distribution, separation and reattachment angles are approximated by characteristic points of mean pressure distributions according to the methodology of Niemann (1971). This estimation of separation/reattachment points thanks to pressure distributions has also been noticed in Section 3.2.

From these definitions and above figures, Table 4.3 summarizes separation and reattachment angles for both cylinders in both flow regimes. URANS simulations predict pretty high values of separation angles regarding the upstream cylinder while experimental ones are lower. According to experimental data, separation angles on the upstream cylinder are lower for rough than smooth cylinders due to the growing instabilities in the turbulent BL and the increase of momentum deficit. However, URANS simulations do not capture this effect. Furthermore, according to Achenbach (1971), who studied the flow around a rough single-cylinder, higher separation angles should appear on the upstream cylinder for the postcritical regime than the subcritical one, but it is not what results from URANS simulations. This wrong estimation in the separation angle in the subcritical regime, leading to a narrower wake, explains why URANS simulations predict a smaller drag coefficient in the subcritical regime than in the postcritical one.

Regarding the downstream cylinder, as instabilities of BL are growing with roughness, the reattachment angle on the downstream cylinder should be higher than in the smooth case. This effect is observed for the postcritical regime but not for the subcritical one. However, reattachment points are in good agreement with Dubois and Andrianne (2021) data. After that, URANS simulations correctly estimate the downstream cylinder separation angle, leading to quite correct estimations for the drag coefficient as highlighted in Table 4.2. Finally, for URANS predictions, a higher downstream cylinder separation angle is observed for the subcritical regime as the flow reattaches at a higher angle. This difference is not present in experimental data, concluding that the separation angle is similar for both regimes on the downstream cylinder. However, it should be reminded that the pressure coefficients are extracted every 7.5 degrees by Dubois and Andrianne (2021), which does not lead to accurate separation points. Also, it is reminded that experimental data are not retrieved from skin friction distribution over the cylinders and should be considered prudently.

Coeff.	URANS	URANS	Dubois and Andrianne (2021)	Dubois and Andrianne (2021)
Re [-]	4.5×10^4	3.95×10^5	4.5×10^4	3.95×10^5
θ_{s_1} [deg]	97	84	75	90
θ_r [deg]	69	66	75	75
θ_{s_2} [deg]	123	115	120	120

Table 4.3: Separation and reattachment positions for rough tandem cylinders from URANS and experimental results.

Wake profiles

Similarly to the smooth case, velocity and TKE profiles are analyzed to highlight differences induced by the roughness in the two different flow regimes. No experimental data are provided by Dubois and Andrianne (2021). A simplified sketch of the tandem is also presented to show where the profiles are plotted. Again, the presented results come from Dubois and Andrianne (2021) simulated experiments. Mean streamwise velocity and TKE profiles along the centerline in Figure 4.8 highlight the wake differences of both cases. In fact, in Figure 4.8 (a), it can be seen that the recirculation length for the postcritical regime ($L_r/D = 0.7$) is lower than the one of subcritical case ($L_r/D = 1$). This can be explained by the differences in total drag coefficient (*cfr.* Table 4.2) and in the downstream separation angles (*cfr.* Table 4.3). Regarding the TKE profiles in Figure 4.8, lower values are reached for the postcritical flow, and the associated TKE decay occurs more quickly. Compared to the smooth case in Figure 3.7 (b), the TKE decay occurs more quickly for the present rough considerations.

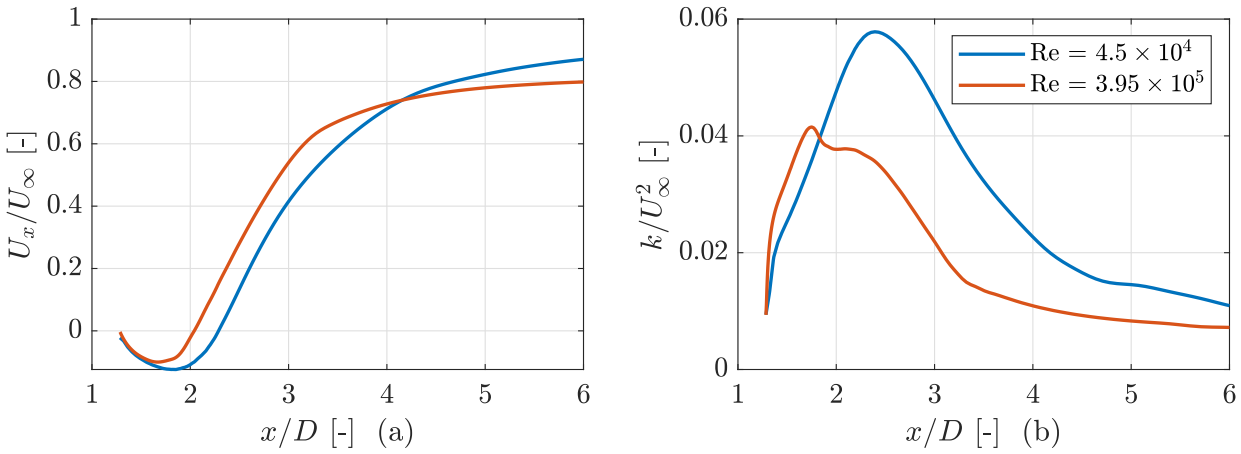

Figure 4.8: Comparison of the mean streamwise velocity (U_x) and mean TKE (k) along the centerline in the downstream cylinder wake for the two simulated experiments of Dubois and Andrianne (2021).

Regarding the mean streamwise and vertical velocity profiles along the vertical coordinate in Figure 4.9, as in the smooth case, differences are more visible outside the recirculation region. Inside the recirculation region, in Figure 4.9 (a)-(b), the regime does not affect the profiles a lot as they are very similar with a negative mean streamwise velocity at $y/D = 0$. Furthermore, the presented allures are very similar to the smooth profile of Figure 3.8. However, compared to the smooth case where three changes of the sign were observed for the vertical velocity, only one change is observed for both regimes in the rough case.

By analyzing mean velocity profiles outside the recirculation region, it can be observed that higher differences appear between both regimes. A wider wake appears for the postcritical regime, as it can be seen in Figure 4.9 (c), leading to a higher total drag coefficient in Table 4.2. However, this effect does not follow experimental results as mentioned by the analysis of Table 4.2. After that, lower values of U_x/U_∞ can be observed in the subcritical case as the recirculation length is not the same for both regimes in the rough case. Small asymmetries can also be observed for the subcritical profiles in Figure 4.9 (c)-(d). They are due to not sufficiently accurate time-averaging procedure and do not attest to flow asymmetry. Regarding the vertical velocity profile in Figure 4.9 (d), as in the smooth case, one change of sign is observed at the centerline. The vertical velocity component decreases when computed outside the recirculation region as the vortices strength gradually decreases.

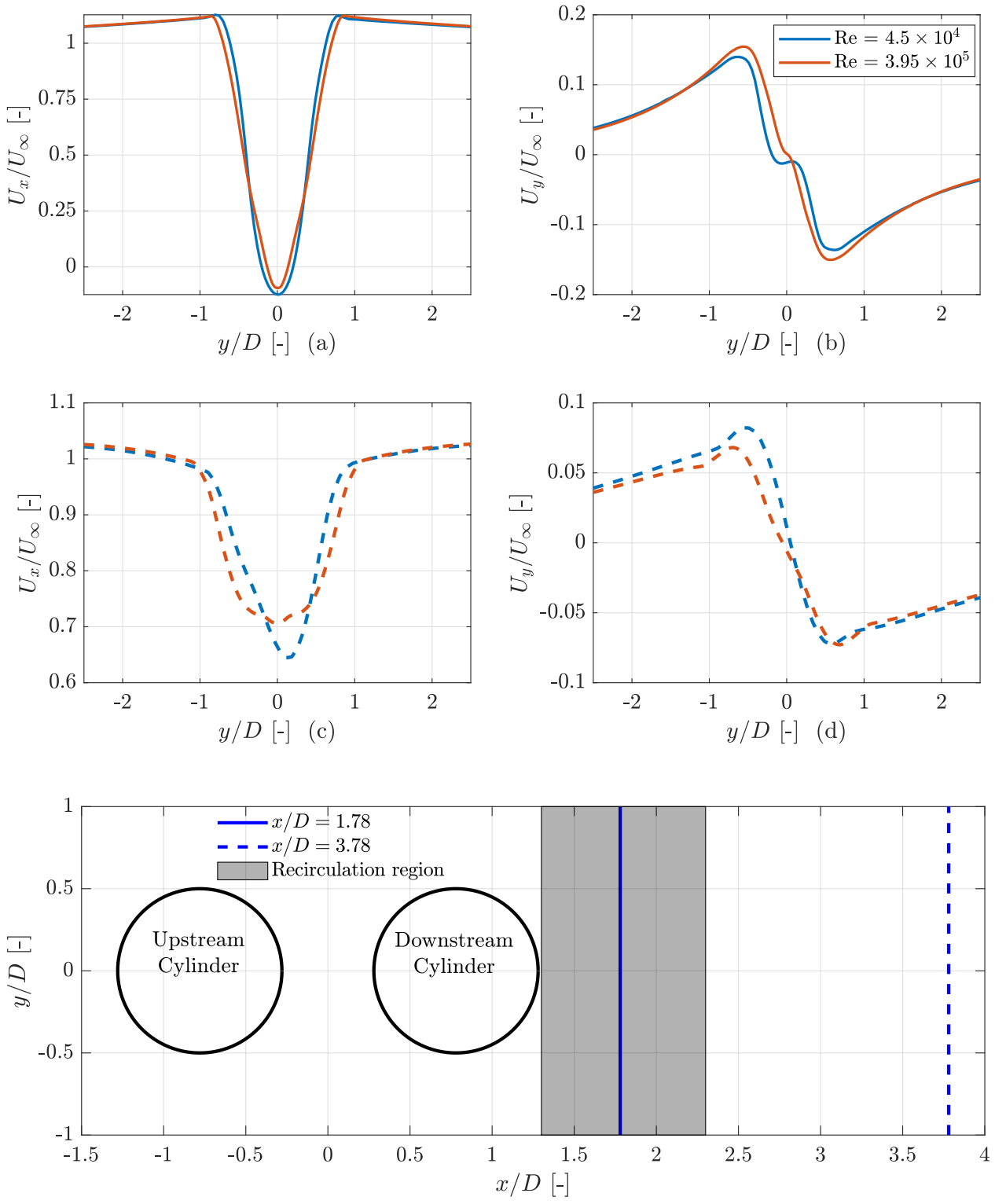

Figure 4.9: Comparison of the mean streamwise and vertical velocities profiles in the downstream cylinder wake for the two simulated experiments of Dubois and Andrianne (2021). $x/D = 1.78$ (solid line) and $x/D = 3.78$ (dotted line).

4.3. Roughness effects

This section analyzes the effects of roughness in both the subcritical and postcritical regimes. The parameters of Schewe and Jacobs (2019) experiments are used (*cfr.* Table 3.1 in Section 3) and the roughness is introduced. Two Reynolds numbers are considered: $\mathrm{Re} = 1.66 \times 10^5$ and $\mathrm{Re} = 5 \times 10^6$ for the subcritical and postcritical regimes, respectively. Regarding the roughness, the value K_s/D is varied from 10^{-6} until 5×10^{-3} and the constant C_s is set to 0.5 to consider uniform roughness. The roughness range allows considering many applications and industrial coating. As highlighted in the previous comparisons with the results of Dubois and Andrianne (2021), the subcritical results must be considered with prudence as wall functions fail to capture some physics for that regime.

Figure 4.10 compares effects of roughness on both regimes thanks to the evolution of different quantities: mean and fluctuating coefficients, separation and reattachment angles, and base pressure coefficients. Compared to the same smooth experiment results of Table 3.4 in Section 3.3, the present results show discrepancies for quasi smooth cylinders ($K_s/D = 10^{-6}$). These discrepancies can be explained by the fact that one case is a resolved wall (results of Table 3.4), and another one has been applied wall functions BCs (current section). After that, as noticed in Section 4.1, the flow at $\mathrm{Re} = 1.66 \times 10^5$ is close the critical regime. Consequently, if roughness reaches a sufficiently high value, the flow will no longer lie in the subcritical regime.

As shown in Figure 4.10, more significant differences appear in the postcritical regime than in the subcritical regarding all the quantities when roughness is increased. The most significant changes concern the downstream cylinder fluctuating lift coefficient, where vortex shedding occurs, and the upstream cylinder base pressure, mainly affecting the downstream cylinder drag coefficient. By analyzing Figure 4.10 (a)-(b) in more depth, it can be noticed that, first, the upstream drag increases while the downstream drag decreases with the roughness. This effect is, as mentioned, more meaningful for the postcritical regime. Also, for the postcritical flow regime, the Strouhal number decreases. After that, in Figure 4.10 (c)-(d), fluctuating parts of aerodynamic coefficients are constant for the subcritical regime while they are increasing for the postcritical regime. The changes in Figures 4.10 (a)-(b) can be explained by the evolution of the separation angles for both cylinders. Indeed, as the upstream cylinder separation angle decreases in Figure 4.10 (f), a wider wake is created, yielding a higher momentum deficit. As a consequence of the wider wake, the reattachment angle moves downstream on the downstream cylinder. This delay in the reattachment position induces a lower drag coefficient, i.e., more negative, as explained in Section 3.3. For both regimes, the downstream cylinder separation angle is not affected by the roughness as the associated BL is highly turbulent. Finally, as shown in Figure 4.10, the base pressure of the upstream cylinder decreases, with a higher decrease in the postcritical regime. This latter decrease is a direct consequence of the earlier separation point. The downstream cylinder base pressure remains constant when roughness is increased as the separation point on the downstream cylinder does not change with roughness.

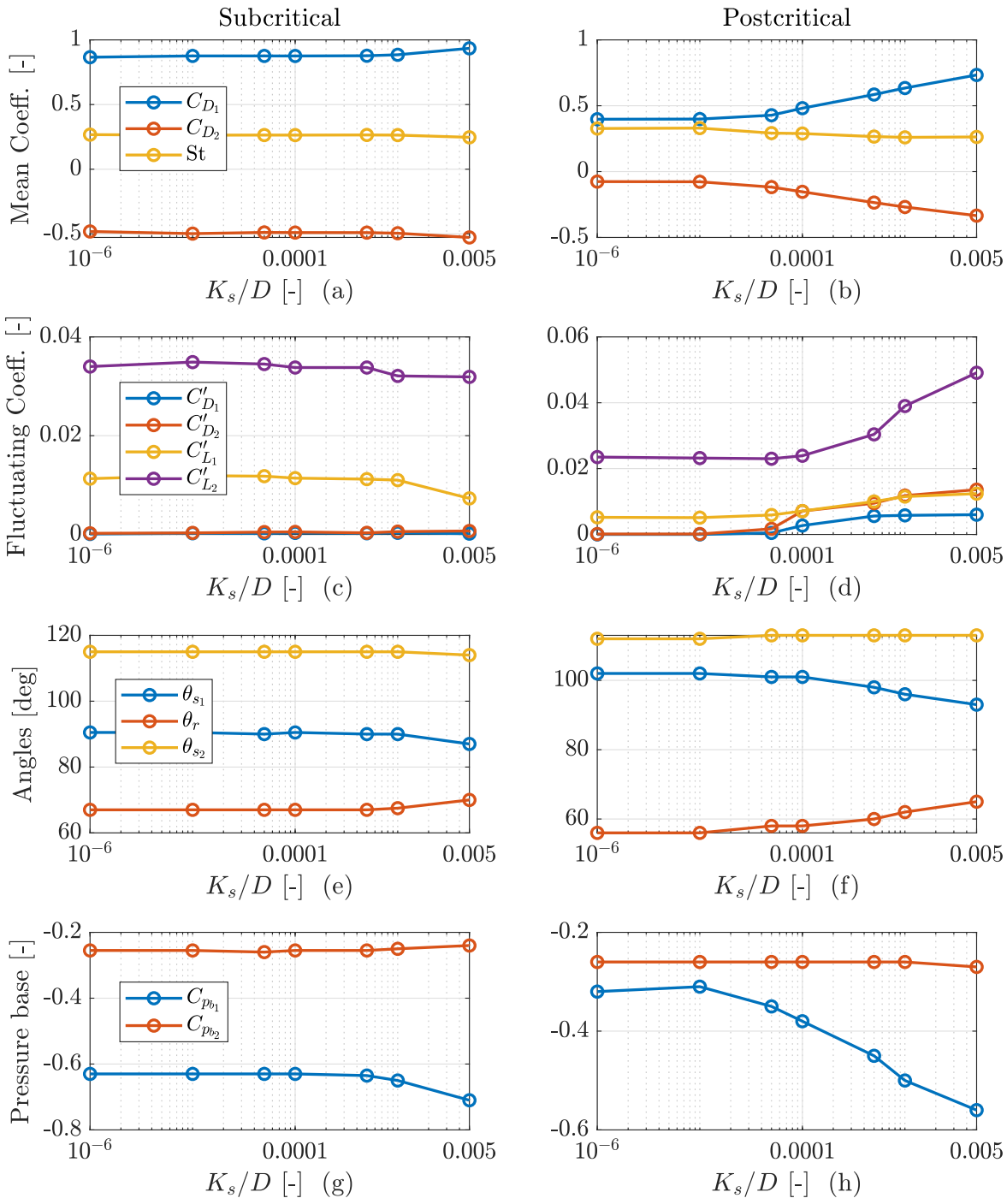

Figure 4.10: Impacts of roughness on mean and fluctuating coefficients [-], separation and reattachment angles [deg], and base pressure coefficients [-]. The left figures stand for the subcritical regime and the right figures for the postcritical regime.

The roughness effects being studied, the study focuses on the experiment of Achenbach (1971). The latter studied the flow around rough single-cylinders in different flow regimes and different levels of roughness. Consequently, only the results of the upstream cylinder of URANS simulations are compared. As for the smooth case of Achenbach (1968), Achenbach (1971) extracted the mean pressure and skin friction coefficient distributions. The main drawback of its experiment is the non-correction of the results while the blockage ratio is high (16 %). Two Reynolds numbers and two levels of roughness are considered. Tables 4.4 and 4.5 summarize the mean drag coefficient and the angle of separation for $K_s/D = 0.001$ and $K_s/D = 0.005$ at $\mathrm{Re} = 1.66 \times 10^5$ and 5×10^6, respectively.

By analyzing Table 4.4, at $\mathrm{Re} = 1.66 \times 10^5$, it can be seen that experimental results predict a drag crisis for $K_s/D = 0.001$, while URANS simulations do not capture this drag crisis for this roughness value. Consequently, URANS simulations do not capture the critical behavior of the flow for that Reynolds number. Although the studied system is tandem and not single, this cannot explain the present discrepancies. A higher drag is observed for experimental data for $K_s/D = 0.005$. URANS simulations are in good agreement regarding this drag coefficient. For the separation angles, the same orders of magnitude are observed between experiments and numerical simulations. However, URANS predict quasi the same separation angle while experiments show a higher one when roughness increases. Roughness alters the flow behavior and triggers the laminar-to-turbulent transition leading to an increase of separation angle for $K_s/D = 0.005$. The friction drag percentage is also presented in Table 4.4 and is overestimated by URANS simulations for $K_s/D = 0.001$ while it is in better agreement with Achenbach (1971) for $K_s/D = 0.005$. Globally, as expected, friction drag percentage is higher for rough than smooth cylinders as for the single as the tandem configurations.

Coeff.	URANS	URANS	Achenbach (1971)	Achenbach (1971)
K_s/D [-]	0.001	0.005	0.001	0.005
C_D [-]	0.88	0.93	0.51	0.87
θ_s [deg]	86	87	90	98
$C_{D_{f,1}}/C_{D_1}$ [%]	6	2.5	1	2

Table 4.4: Upstream cylinder mean drag coefficient [-], separation angles [deg] and friction drag percentage for two roughness values at $\mathrm{Re} = 1.66 \times 10^5$. Single-cylinder data of Achenbach (1971) are introduced for comparison.

Regarding results at $\mathrm{Re} = 5 \times 10^6$, where the regime is considered postcritical, URANS simulations underestimate both drag coefficients. However, they capture the main trend of Achenbach (1971), i.e., an increase of the drag coefficients with roughness in the postcritical regime. In the smooth case, the drag coefficient is expected to remain more or less constant in the postcritical regime. It is not the case for a single-cylinder and the upstream cylinder of a tandem configuration. URANS simulations agree with experimental results regarding the separation angles as they both predict an earlier separation as the roughness increases. As the flow regime is the same for both roughness, i.e., a fully turbulent BL, roughness creates instabilities and a momentum deficit leading to earlier separation, Rodríguez et al. (2016). Finally, friction drag percentage increases with roughness in the postcritical regime as confirmed by URANS simulations and experimental results of Achenbach (1971). As for $\mathrm{Re} = 1.66 \times 10^5$ but in a lesser extent at $\mathrm{Re} = 5 \times 10^6$, URANS simulations overestimate this percentage.

Coeff.	URANS	URANS	Achenbach (1971)	Achenbach (1971)
K_s/D [-]	0.001	0.005	0.001	0.005
C_D [-]	0.63	0.73	0.87	0.98
θ_s [deg]	96	93	100	94
$C_{D_{f,1}}/C_{D_1}$ [%]	2.6	4.1	2	2.7

Table 4.5: Upstream cylinder mean drag coefficient [-], separation angles [deg] and friction drag percentage for two roughness values at $\mathrm{Re} = 5 \times 10^6$. Single-cylinder data of Achenbach (1971) are introduced for comparison.

As drag coefficients and separation angles have been compared, the study focuses on mean pressure and skin friction coefficient distributions over the upstream cylinder. Data of Achenbach (1971) are introduced. For the subcritical regime, as can be seen in Figure 4.11, discrepancies appear between URANS and experimental results for the pressure distribution, especially near the expected minimum of pressure coefficient. However, the base pressure is approximated correctly by URANS, particularly for $K_s/D = 0.001$. URANS simulations tend to conclude that higher friction is expected for lower roughness values regarding the friction coefficient. This effect is non-physical as roughness introduces higher friction whatever the flow regime, see Achenbach (1971). Regarding the angles of separation in the subcritical regime, it is reminded that they are underestimated for both roughness values by URANS simulations as mentioned by Table 4.4. Although URANS simulations consider the upstream cylinder of tandem cylinders and Achenbach (1971) considered a single-cylinder, this cannot explain the present divergences. Again, wall functions are the main causes of high discrepancies with experimental results at low Reynolds number.

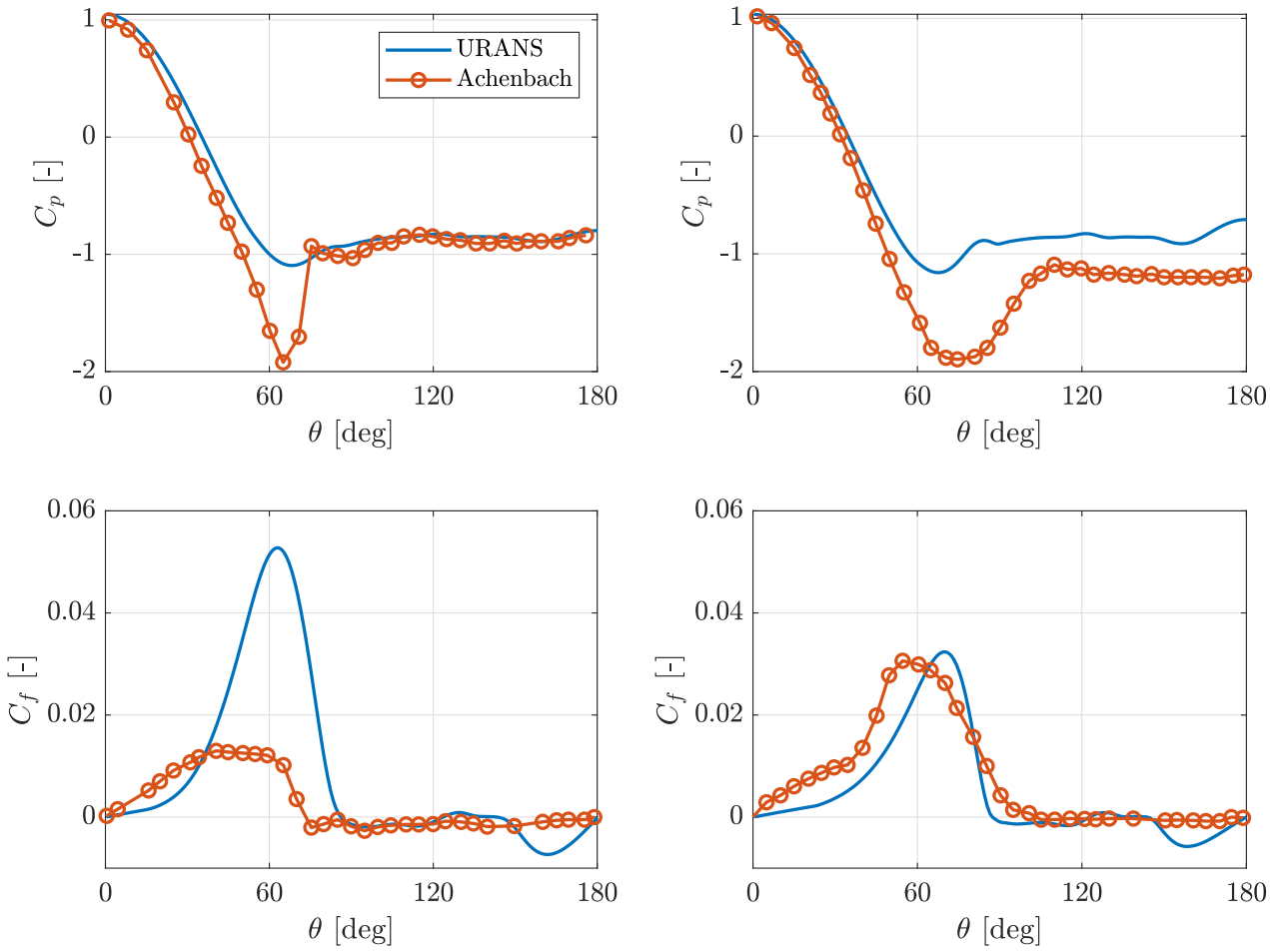

Figure 4.11: Mean pressure and skin friction coefficients distribution on the upstream cylinder at Re $= 1.66 \times 10^5$. Two roughness values are introduced: $K_s/D = 0.001$ (left figures) and $K_s/D = 0.005$ (right figures).

Regarding the postcritical mean pressure and skin friction comparison, more similar results are observed between URANS simulations and experimental results of Achenbach (1971). Indeed, as presented in Figure 4.12, similar behaviors of pressure coefficients are observed for both roughnesses. The minimum of pressure coefficients appears at the same angular position with slight amplitude differences. Also, a difference appears in the base pressure, which highly affects the drag coefficients. These differences in amplitude can be attributed to the high blockage ratio and the non-correction of the results. This leads to different drag coefficients in Table 4.5 between URANS and experimental results. As shown in Table 4.5, separation angles and friction drag percentage are in good agreement. This is confirmed by skin friction coefficient distributions in Figure 4.12, which are very similar for URANS models and experiments. Differences appear at the rear cylinder as Achenbach (1971) studied a single-cylinder, while a more recirculating region is present behind the upstream cylinder of the tandem, coming from the downstream cylinder. As for the smooth case, wall functions presented accurate approximations of experimental results for sufficiently high Reynolds numbers. For rough cylinders

in the postcritical regime, URANS simulations confirm that high similarities in pressure and skin friction distributions exist between the upstream cylinder of a tandem of cylinders and a single-cylinder.

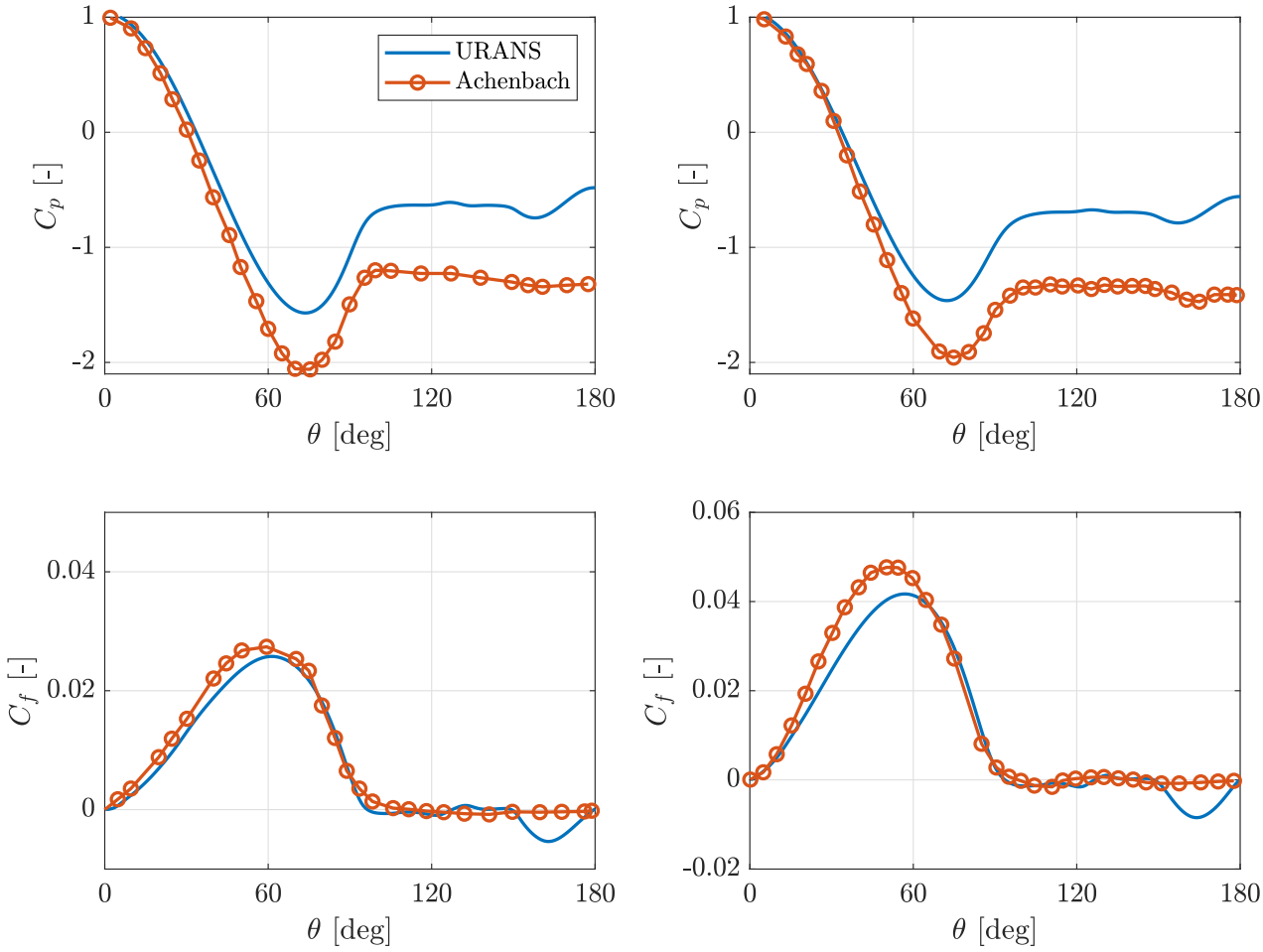

Figure 4.12: Mean pressure and skin friction coefficients distribution on the upstream cylinder at Re $= 5 \times 10^6$. Two roughness values are introduced: $K_s/D = 0.001$ (left figures) and $K_s/D = 0.005$ (right figures)

4.4. Flow topologies

This subsection summarizes the flow topology in the four studied cases: smooth and rough tandem cylinders in both the subcritical and postcritical regimes. S/D is kept to 1.56, and the Reynolds numbers for smooth cases are 1.66×10^5 and 5×10^6 for the subcritical and postcritical regimes, respectively. For the rough case, K_s/D is set to 0.005, and the Reynolds numbers are set to 4.5×10^4 and 5×10^6 for the subcritical and postcritical regimes, respectively.

The instantaneous contours of vorticity along the z-direction (Ω_z) are plotted to analyze the flow topologies. 44 values of vorticity going from -550 to 550 with an exponential distribution are represented. For each of the four cases, 5 instantaneous contours are represented. They allow considering the flow behavior during an entire period. The latter is based on the lift coefficient of the downstream cylinder.

Figure 4.13 presents vorticity contours for the subcritical flow around smooth tandem cylinders. As it can be seen, the flow behavior in the gap cylinders does not lead to vortex shedding and is formed of two stationary vortices with the same magnitude but opposite in sign. The flow behavior between the two cylinders does not fluctuate in time. The main temporal changes appear in the downstream cylinder wake, where vortex shedding occurs. The separated shear layers from the upstream cylinder reattach on the downstream one and finally separate in the backward direction. In addition to the present observations, Alam et al. (2003) also reported a separation in the forward direction on the downstream cylinder. This effect has not been noticed yet for URANS results but seems to take place by analyzing Figure 4.13. Alam et al. (2003) also concluded that the flow reattaches around $\theta = 174°$ on the upstream cylinder for $S/D < 1.5$. As $S/D = 1.56$ for the present simulations, this effect does not take place, as confirmed by the absence of forward reattachment on the upstream cylinder in Figure 4.13.

Compared to the subcritical regime case, the postcritical regime yields the same conclusion for the flow behavior as confirmed by Figure 4.14. As explained in Section 3.3, the overall wake is narrower for the postcritical regime, as confirmed here. Also, the separation on the upstream cylinder is delayed due to the turbulent BL. The vortices behind the downstream cylinder are weaker for the postcritical regime, but as Strouhal numbers of both regimes are pretty similar (*cfr.* Table 3.4 in Section 3.3), the vortex behavior is the same than in the subcritical regime.

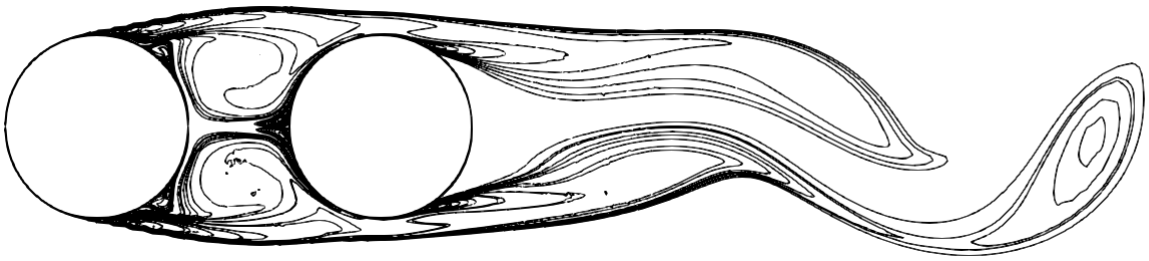

(a) $tU_\infty/D = 0.2/\mathrm{St}$

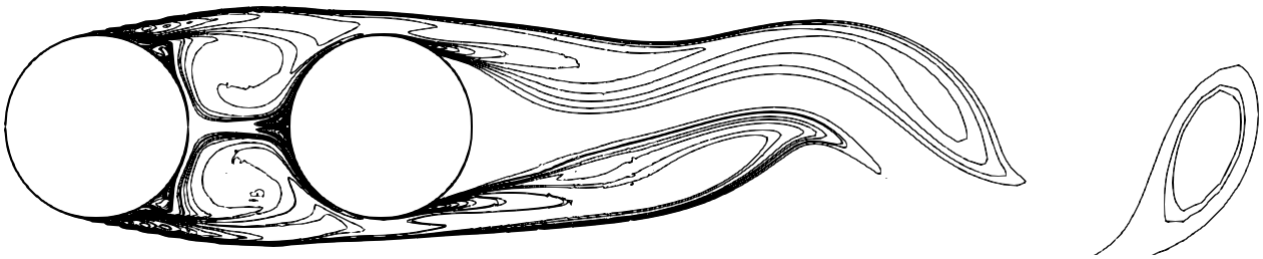

(b) $tU_\infty/D = 0.4/\mathrm{St}$

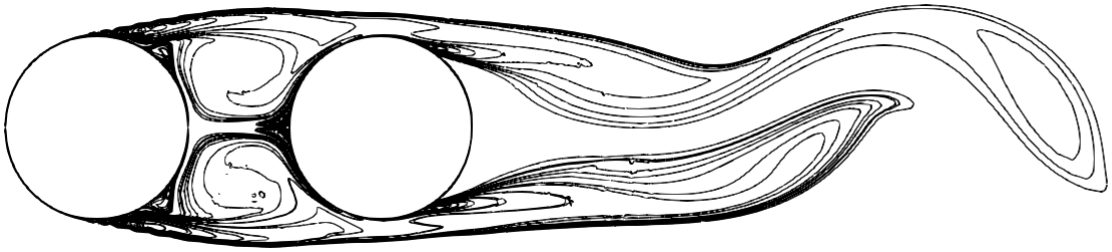

(c) $tU_\infty/D = 0.6/\mathrm{St}$

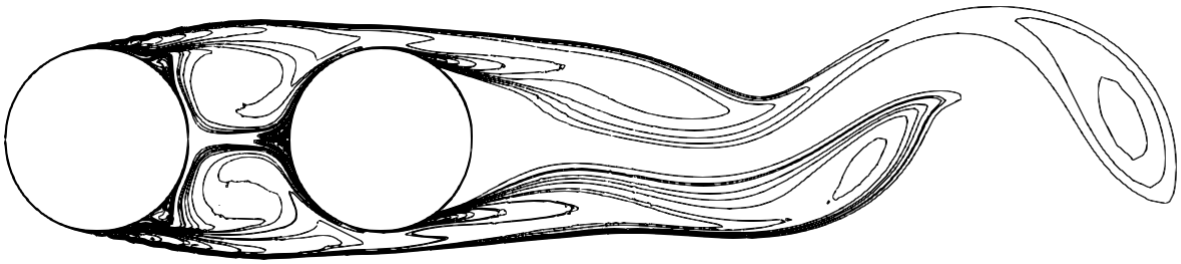

(d) $tU_\infty/D = 0.8/\mathrm{St}$

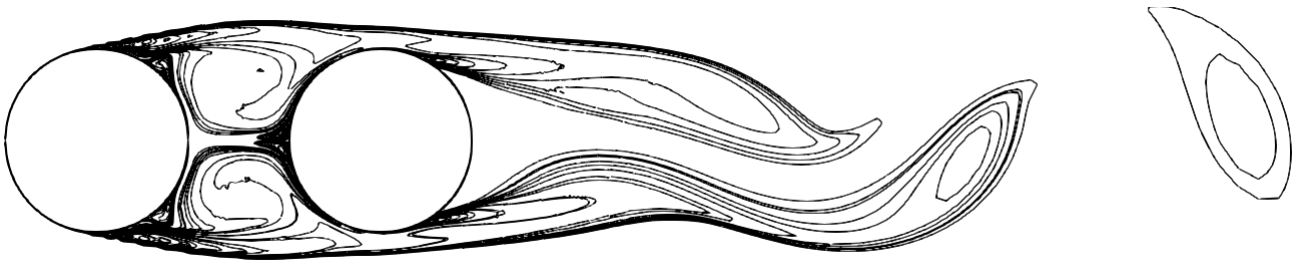

(e) $tU_\infty/D = 1/\mathrm{St}$

Figure 4.13: Instantaneous vorticity contours along z ($\Omega_z D/U_\infty$) for smooth tandem cylinders in the subcritical regime.

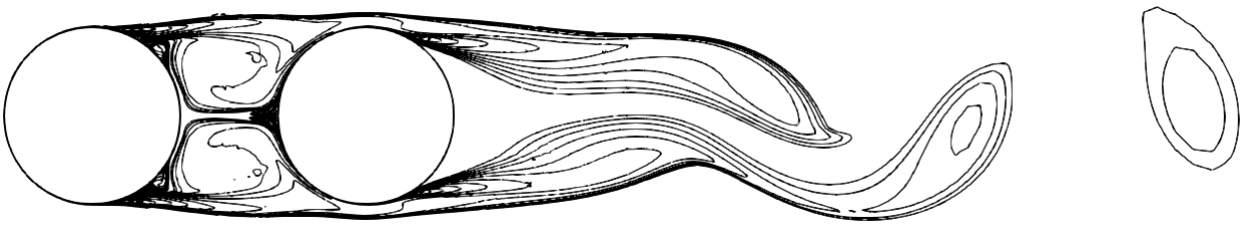

(a) $tU_\infty/D = 0.2/\mathrm{St}$

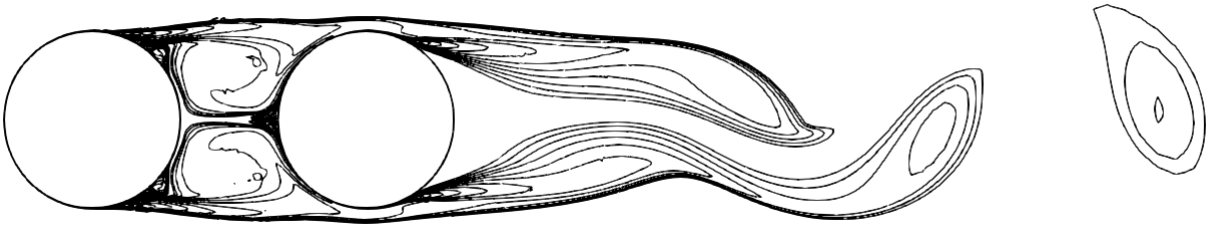

(b) $tU_\infty/D = 0.4/\mathrm{St}$

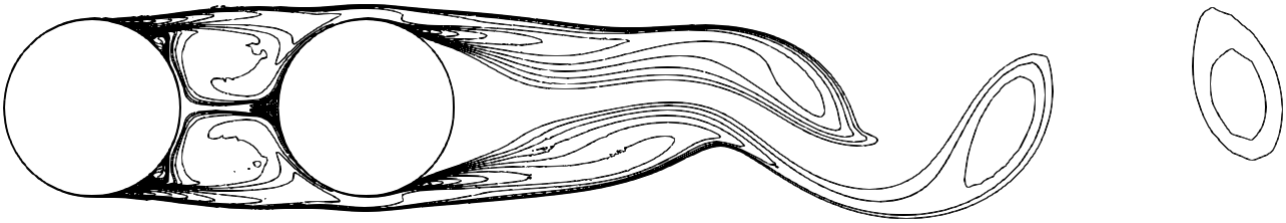

(c) $tU_\infty/D = 0.6/\mathrm{St}$

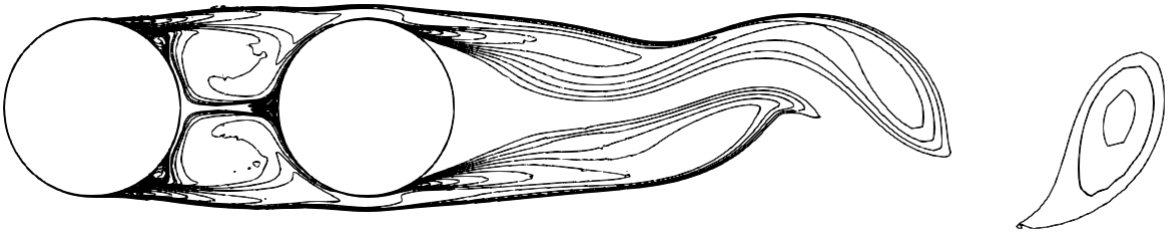

(d) $tU_\infty/D = 0.8/\mathrm{St}$

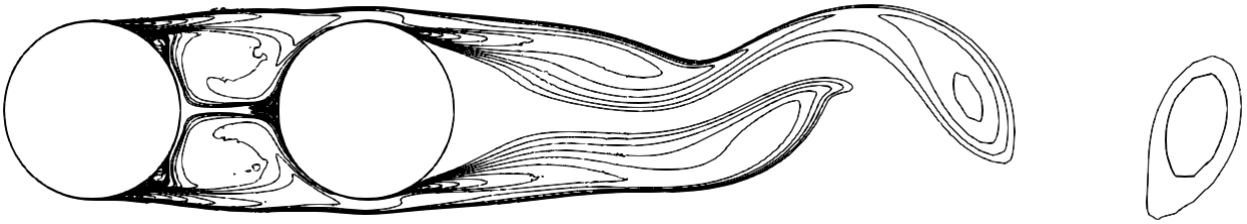

(e) $tU_\infty/D = 1/\mathrm{St}$

Figure 4.14: Instantaneous vorticity contours along z ($\Omega_z D/U_\infty$) for smooth tandem cylinders in the postcritical regime.

Compared to the smooth case, the subcritical flow around rough cylinders presents the same flow behavior: the separated shear layers reattach on the downstream cylinder and finally separate in the backward direction. The forward separation on the downstream cylinder, reported previously, is less evident in the rough case. Roughness yields higher temporal fluctuations for the flow in the cylinder gap than for the smooth case, as can be seen in Figure 4.15. The latter fluctuations induce more significant temporal changes in the reattachment and separation points on the downstream cylinder. Also, the flow separation is triggered by roughness on the upstream cylinder, while a delay is observed on the downstream cylinder. Globally, as roughness level is high, significant vorticity magnitudes are observed in the BLs and the separated shear layers, yielding a wider wake than in the smooth case. However, the present flow behavior must be considered with extreme prudence as wall function yield bad results for the subcritical regime.

Compared to the three previous cases, the postcritical flow around a tandem of rough cylinders presents the same flow behavior, as confirmed by Figure 4.16. However, much lower flow fluctuations are observed in the cylinders gap than the subcritical flow for rough cylinders. As indicated in Section 4.3, the separation is delayed on the upstream cylinder, leading to narrower wake. However, as the roughness level is significant ($K_s/D = 0.005$) and the Reynolds number is high ($\mathrm{Re} = 5 \times 10^6$), a higher friction drag percentage is found for the postcritical regime. This leads to larger vortex areas in the wake, as can be seen in Figure 4.16.

Dubois and Andrianne (2021) also described the flow behavior on rough cylinders. In addition to the present observations, they also reported a reattached zone on the downstream cylinder in the forward direction for both flow regimes. The latter reattachment is followed by a separated flow around $\theta = 30°$. For $S/D < 1.56$, this separated flow reattaches on the upstream cylinder around $\theta = 180°$. The present results of the URANS simulations do not allow stating on the forward separation behavior reported by Dubois and Andrianne (2021).

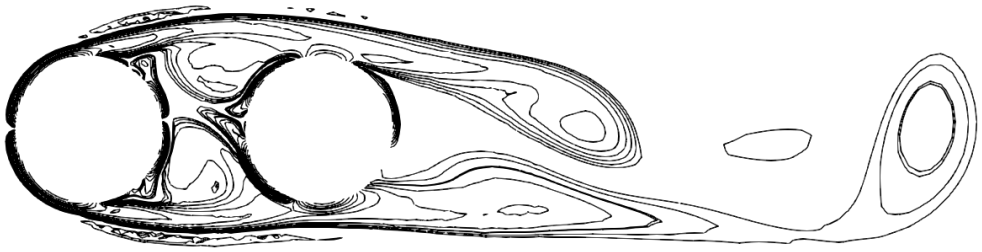

(a) $tU_\infty/D = 0.2/\mathrm{St}$

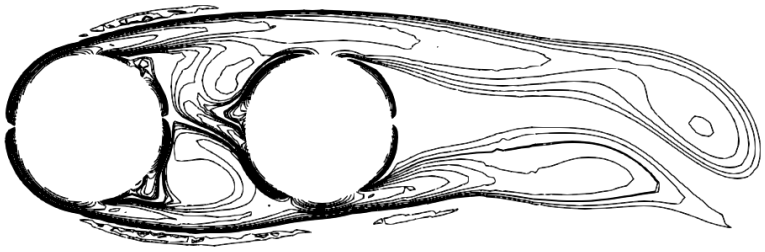

(b) $tU_\infty/D = 0.4/\mathrm{St}$

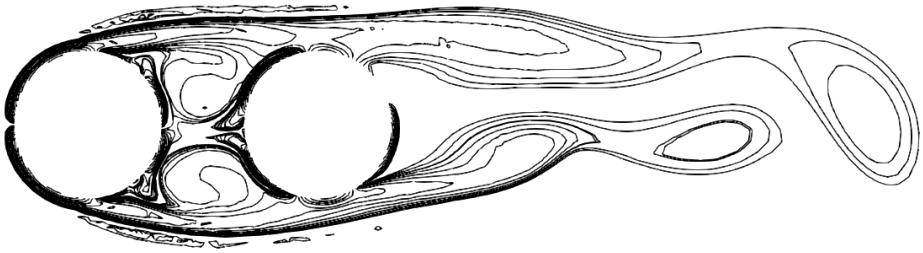

(c) $tU_\infty/D = 0.6/\mathrm{St}$

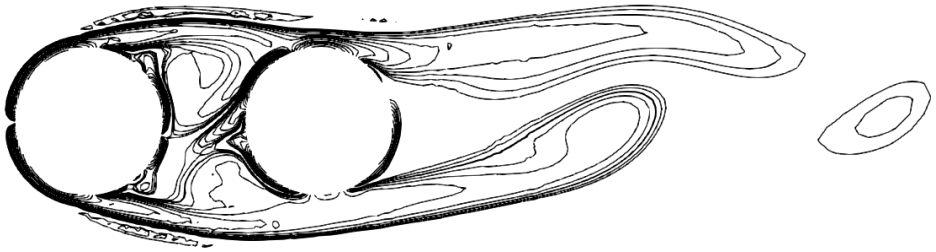

(d) $tU_\infty/D = 0.8/\mathrm{St}$

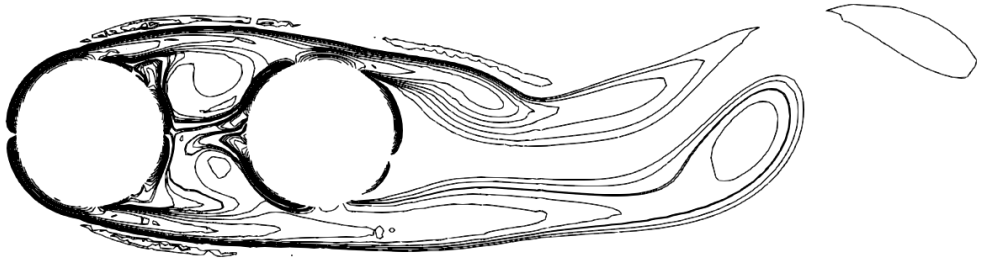

(e) $tU_\infty/D = 1/\mathrm{St}$

Figure 4.15: Instantaneous vorticity contours along z ($\Omega_z D/U_\infty$) for rough tandem cylinders in the subcritical regime.

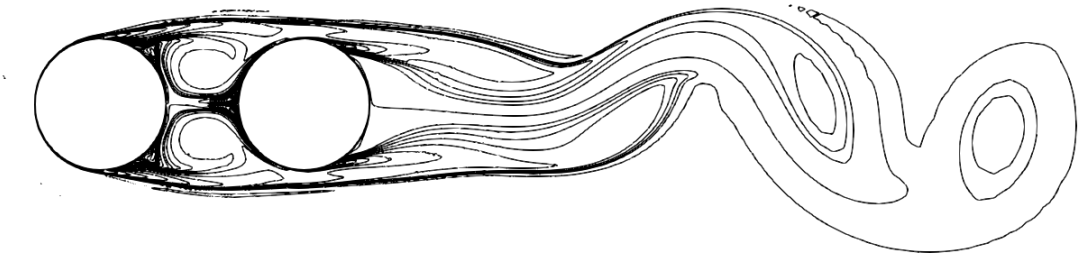

(a) $tU_\infty/D = 0.2/\mathrm{St}$

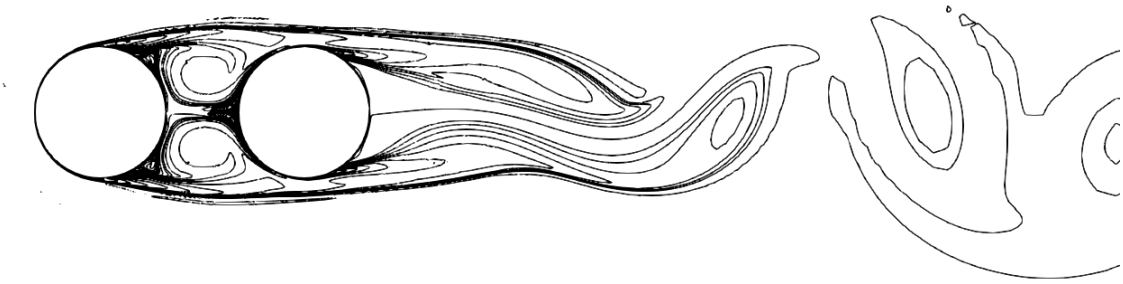

(b) $tU_\infty/D = 0.4/\mathrm{St}$

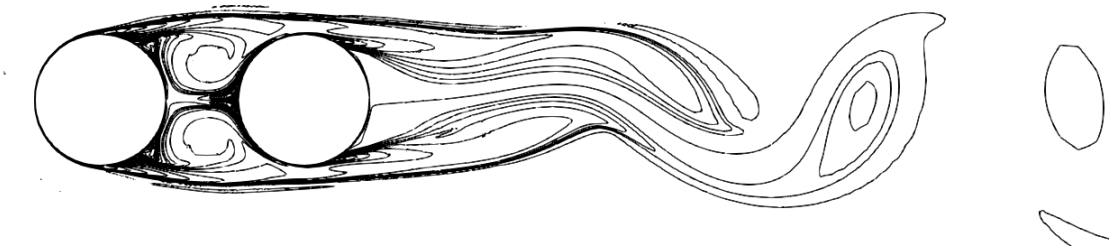

(c) $tU_\infty/D = 0.6/\mathrm{St}$

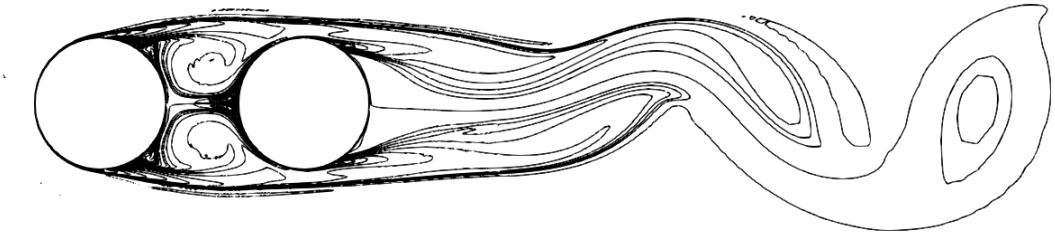

(d) $tU_\infty/D = 0.8/\mathrm{St}$

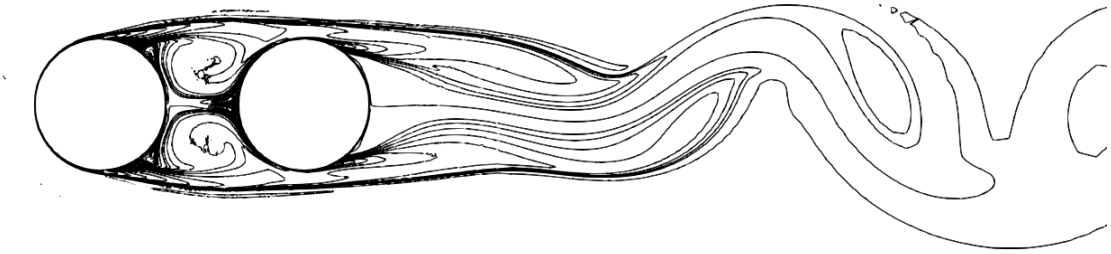

(e) $tU_\infty/D = 1/\mathrm{St}$

Figure 4.16: Instantaneous vorticity contours along z ($\Omega_z D/U_\infty$) for rough tandem cylinders in the postcritical regime.

5. Conclusions

This section intends to summarize the main results and provides some perspectives for future works on numerical simulations.

5.1. Summary

Throughout this thesis, two-dimensional numerical simulations have been carried out to assess the ability of URANS formulation to capture the main quantities of the flow around smooth and rough static tandem cylinders. The subcritical and postcritical regimes and very low center-to-center spacing between both cylinders have been considered. Two turbulence models have been introduced: the $k-\omega$ SST model and the Langtry-Menter 4-equation Transitional SST model. The use of wall functions BCs has also been assessed. From preliminary studies on the flow around a smooth single-cylinder, the $k-\omega$ SST model with a resolved viscous sublayer is more adapted for the subcritical regime, where the BL remains laminar before separation. At the same time, the transition model is more adapted with wall functions, which reduce the CPU resources, for the postcritical regime where the flow separation is delayed on the upstream cylinder. Regarding the roughness, it is only modeled by wall functions and the use of $k-\omega$ SST closure, irrespective of the regime. This choice is made as the transition model is inefficient with wall functions.

To validate the previous choices, simulations of the flow around smooth cylinders in the subcritical regime have been performed at $\mathrm{Re} = 6.5 \times 10^4$ and compared to the results of Alam et al. (2003). URANS showed excellent approximations of both the mean and fluctuating quantities. However, the experimentally observed forward reattachment on the upstream cylinder was not captured by URANS simulations. For the postcritical regime validation, the literature lacks experiments. However, the mean force coefficients of the experiments of Schewe and Jacobs (2019) were correctly estimated for this regime. From both regime comparisons in the smooth case, the main differences lie in the lower fluctuating forces for the postcritical regime and the delay in the turbulent BL separation on the upstream cylinder. The latter effect induces an earlier reattachment on the downstream cylinder, a lower global momentum deficit, and a narrower wake.

Regarding the main results, a Reynolds effect study has been performed between $\mathrm{Re} = 4.5 \times 10^4$ and 2×10^5. Changes were observed around $\mathrm{Re} = 1.4 \times 10^5$, where fluctuating forces of both cylinders suddenly drop. Also, at this Reynolds number, the Strouhal number switches from 0.12 to 0.28. Around $\mathrm{Re} = 1.6 \times 10^5$, the drag coefficient of the upstream cylinder decreases. At $\mathrm{Re} = 2 \times 10^5$, the flow regime is critical, which underestimates the critical Reynolds of experimental results. For the upstream cylinder, the higher the Reynolds number is, the higher the separation angle is. Providing that $\mathrm{Re} < 2 \times 10^5$, the BL remains laminar until separation. Regarding the downstream cylinder, the higher the Reynolds number is, the lower the

reattachment position is. The separation on the downstream cylinder does not vary with Re and is fully turbulent.

Concerning the flow around rough cylinders, experiments of Dubois and Andrianne (2021) were simulated. They allowed highlighting the wrong results induced by wall functions when dealing with the flow around cylinders in the subcritical regime. Concerning the postcritical regime, more physical results were observed from simulations, but some quantity estimations were not as accurate as in the smooth case. A roughness effects study has been performed for both regimes. Globally, roughness induces higher drag, decrease of fluctuating forces, higher instability and consequently triggers the laminar-to-turbulent transition. Also, separation occurs earlier as instabilities are growing. After that, a comparison with Achenbach (1971) at a very high Reynolds number showed that the rough upstream cylinder behaves as a single-cylinder except in the rear where the two stationary vortices, due to the tandem arrangement, have an impact.

Finally, the flow topologies comparison study allowed concluding that irrespective of the roughness value or the flow regime, the separated shear layers from the upstream cylinder reattach on the downstream one and finally separate in the backward direction. Between the two cylinders, two vortices of opposite magnitude are present and do not fluctuate a lot in time, except for the subcritical flow around rough cylinders, where the fluctuations in the cylinder gap are more significant than in the postcritical regime. For all cases, a vortex shedding pattern only appears behind the downstream cylinder with a higher vortices magnitude for rough cases and higher wake fluctuations in the subcritical regime.

5.2. Perspectives

The first perspective for this work is the center-to-center (S/D) effects study for both flow regimes in the smooth case. Indeed, this thesis only focused on very short values of S/D. However, from the literature, significant changes are expected when S/D is increased. URANS formulations dealt with a quasi single-bluff body in this work, induced by small values of S/D, while when S/D is further increased, a more complex flow pattern appears and could not be captured by URANS simulations. Also, different angles of attack of the incoming flow could be tested and could be compared with the results of Schewe and Jacobs (2019). These two changes of geometric parameters (spacing and angle of attack) could conclude the ability of URANS simulations to deal with any tandem configuration.

Given the inaccurate estimation of the flow around rough cylinders, especially in the subcritical regime, other ways to model the roughness must be considered. Indeed, the easiest way to include roughness has been applied in this work, i.e., modify wall function BCs. However, the transition model cannot deal with wall functions BCs and misses the laminar-to-turbulent transition, yielding a fully turbulent BL in the subcritical regime, which is non-physical. Also,

in the postcritical regime, wall functions do not behave as correctly as in the smooth case. In this context, the improvement would be to model the roughness by an accurate design of the grains at the cylinder walls, as performed by Rodríguez et al. (2016). This would require complex meshing methods and higher CPU resources as wall functions could not be used anymore. However, this would ensure that the transition is captured in the subcritical regime and would lead to more physical flow modelization. In the postcritical regime, more physical results could be expected thanks to this roughness grains design.

The present work has covered the static study of tandem cylinders but has not studied what usually occurs in engineering structures: the fluid-structure interaction. Flow-induced vibrations (FIV) analyses have been widely carried out for the single-cylinder system, but the literature lacks FIV studies in the context of tandem cylinders, *a fortiori* for rough cylinders. The FIV studies should at first be performed on rigid cylinders mounted together or not, according to the studied case, and by using fluid elastic modeling. FIV simulations require moving mesh and re-meshing procedures, necessitating more CPU resources.

As a first step in the FIV studies, a more affordable and less expensive model could be introduced: the wake oscillator model. The latter allows describing the fluid-structure interaction by a non-linear system of equations, where the effects of the wake on the cylinders, the effects of the cylinders on the wake, and the dynamics of the free wake appear. Tamura (1981) studied the latter model by assuming the cylinder to be at rest, among others. The system of equations finally yielded a Van Der Pol oscillator in Equation 5.1.

$$\frac{\mathrm{d}^2\alpha(t)}{\mathrm{d}t^2} - \varepsilon\omega_0\left(1-\alpha^2(t)\right)\frac{\mathrm{d}\alpha(t)}{\mathrm{d}t} \dashv \omega_0^2\alpha(t) = 0, \tag{5.1}$$

where ε is the damping factor of the system, ω_0 the motion frequency, and α a fictive point motion behind a single-cylinder. Equation 5.1 is non-linear. In the context of tandem cylinders, α could be decomposed into two variables: $\alpha = (\alpha_1, \alpha_2)$. α_1 would be assimilated, as an example, to the separation angle on the upstream cylinder and α_2 to the reattachment angle on the downstream cylinder. The separation point on the downstream cylinder is not considered as its temporal fluctuations are not significant. By solving numerically Equation 5.1 for α_1 and α_2, it would be possible to access the oscillations of the angles, consequently the wake behavior, and to compare them to URANS predictions. This would be a first step in the wake-structure interactions induced by the flow around tandem cylinders.

References

Achenbach, E. (1968). Distribution of local pressure and skin friction around a circular cylinder in cross-flow up to Re= 5×10^6. *Journal of fluid Mechanics*, 34(4):625–639.

Achenbach, E. (1971). Influence of surface roughness on the cross-flow around a circular cylinder. *Journal of fluid mechanics*, 46(2):321–335.

Alam, M. M., Moriya, M., Takai, K., and Sakamoto, H. (2003). Fluctuating fluid forces acting on two circular cylinders in a tandem arrangement at a subcritical Reynolds number. *Journal of Wind Engineering and Industrial Aerodynamics*, 91(1-2):139–154.

Benidir, A., Flamand, O., Gaillet, L., and Dimitriadis, G. (2015). Impact of roughness and circularity-defect on bridge cables stability. *Journal of Wind Engineering and Industrial Aerodynamics*, 137:1–13.

Breuer, M. (1999). Large eddy simulation of high Reynolds number circular cylinder flow. In *Industrial and Environmental Applications of Direct and Large-Eddy Simulation*, pages 176–189. Springer.

Catalano, P., Wang, M., Iaccarino, G., and Moin, P. (2003). Numerical simulation of the flow around a circular cylinder at high Reynolds numbers. *International journal of heat and fluid flow*, 24(4):463–469.

CECI (2021). *CECI: Consortium des Équipements de Calcul Intensif ,description*. Available `here`, Accessed: 2021-05-20.

Chang, P. K. (2014). *Separation of flow*. Elsevier.

Cousteix, J. (2003). *Aircraft Aerodynamic Boundary Layers*. Elsevier.

Derakhshandeh, J. F., Arjomandi, M., Dally, B., and Cazzolato, B. (2014). The effect of arrangement of two circular cylinders on the maximum efficiency of vortex-induced vibration power using a scale-adaptive simulation model. *Journal of Fluids and Structures*, 49:654–666.

Dong, S. and Karniadakis, G. E. (2005). DNS of flow past a stationary and oscillating cylinder at Re = 10000. *Journal of fluids and structures*, 20(4):519–531.

Dubois, R. and Andrianne, T. (2021). Flow around tandem rough cylinders: effects of spacing and flow regimes. *under revision in the Journal of Fluids and Structures*.

Fage, A. (1929). The effects of turbulence and surface roughness on the drag of a circular cylinder. *Rep, Memo.*, 1.

Fage, A. and Falkner, V. (1931). Further experiments on the flow around a circular cylinder. Technical report, HM Stationery Office.

Garbaruk, A., Shur, M., Strelets, M., Spalart, P., and Balakrishnan, R. (2010). Ddes and iddes of tandem cylinders. *Proceedings of the Benchmark problems for Airframe Noise Computations BANC, vol. anl-10/26. Argonne National Laboratory.*

Gopalan, H. and Jaiman, R. (2015). Numerical study of the flow interference between tandem cylinders employing non-linear hybrid URANS–LES methods. *Journal of Wind Engineering and Industrial Aerodynamics*, 142:111–129.

Han, X., Tang, Y., Meng, Z., Fu, F., Qiu, A., Gu, J., and Wu, J. (2021). Surface roughness effect on cylinder vortex-induced vibration at moderate Re regimes. *Ocean Engineering*, 224:108690.

Hirsch, C. (2007). *Numerical computation of internal and external flows: The fundamentals of computational fluid dynamics*. Elsevier.

Hu, X., Zhang, X., and You, Y. (2019). On the flow around two circular cylinders in tandem arrangement at high Reynolds numbers. *Ocean Engineering*, 189:106301.

Igarashi, T. (1981). Characteristics of the flow around two circular cylinders arranged in tandem: 1st report. *Bulletin of JSME*, 24(188):323–331.

Issa, R. I. (1986). Solution of the implicitly discretised fluid flow equations by operator-splitting. *Journal of computational physics*, 62(1):40–65.

Jenkins, L., Neuhart, D., McGinley, C., Khorrami, M., and Choudhari, M. (2006). Measurements of unsteady wake interference between tandem cylinders. In *36th AIAA fluid dynamics conference and exhibit*, page 3202.

Jones, W. and Launder, B. E. (1972). The prediction of laminarization with a two-equation model of turbulence. *International journal of heat and mass transfer*, 15(2):301–314.

Kalitzin, G., Medic, G., Iaccarino, G., and Durbin, P. (2005). Near-wall behavior of RANS turbulence models and implications for wall functions. *Journal of Computational Physics*, 204(1):265–291.

Langtry, R. B. (2006). A correlation-based transition model using local variables for unstructured parallelized cfd codes.

Langtry, R. B. and Menter, F. R. (2009). Correlation-based transition modeling for unstructured parallelized computational fluid dynamics codes. *AIAA journal*, 47(12):2894–2906.

Liu, F. (June 2016). A Thorough Description Of How Wall Functions Are Implemented In OpenFOAM. *In Proceedings of CFD with OpenSource Software.*

Liu, S. and Qin, N. (2015). Modelling roughness effects for transitional low Reynolds number aerofoil flows. *Proceedings of the Institution of Mechanical Engineers, Part G: Journal of Aerospace Engineering*, 229(2):280–289.

Matteoni, G. and Georgakis, C. (2012). Effects of bridge cable surface roughness and cross-sectional distortion on aerodynamic force coefficients. *Journal of wind engineering and industrial aerodynamics*, 104:176–187.

Menter, F. R. (1994). Two-equation eddy-viscosity turbulence models for engineering applications. *AIAA journal*, 32(8):1598–1605.

Niemann, H. (1971). On the stationary wind loading of axisymmetric structures in the transcritical Reynolds number region. *Konstruktiven Ingenieurbau, Ruhr-Universitat Bochum, Report*, (71-2).

Nikuradse, J. et al. (1950). *Laws of flow in rough pipes*. National Advisory Committee for Aeronautics Washington.

Okajima, A. (1979). Flows around two tandem circular cylinders at very high Reynolds numbers. *Bulletin of JSME*, 22(166):504–511.

Ong, M. C., Utnes, T., Holmedal, L. E., Myrhaug, D., and Pettersen, B. (2010). Numerical simulation of flow around a circular cylinder close to a flat seabed at high Reynolds numbers using a $k - \varepsilon$ model. *Coastal Engineering*, 57(10):931–947.

OpenFOAM (December 2020). *The open Source CFD Toolbox: User guide. Version v2012*. OpenCFD Limited. Available `here`.

Owen, S. J. (1998). A survey of unstructured mesh generation technology. *IMR*, 239:267.

Rodríguez, I., Lehmkuhl, O., Piomelli, U., Chiva, J., Borrell, R., and Oliva, A. (2016). Numerical simulation of roughness effects on the flow past a circular cylinder. *Journal of Physics: Conference Series*, 745(3):032043.

Rosetti, G. F., Vaz, G., and Fujarra, A. L. (2012). URANS calculations for smooth circular cylinder flow in a wide range of Reynolds numbers: solution verification and validation. *Journal of Fluids Engineering*, 134(12).

Roshko, A. (1961). Experiments on the flow past a circular cylinder at very high Reynolds number. *Journal of fluid mechanics*, 10(3):345–356.

Schewe, G. and Jacobs, M. (2019). Experiments on the flow around two tandem circular cylinders from sub-up to transcritical Reynolds numbers. *Journal of Fluids and Structures*, 88:148–166.

Schlichting, H. and Gersten, K. (1979). Boundary-layer theory, (2000). *International Journal of Aerospace Engineering Hindawi www. hindawi. com*, 2018.

Stringer, R., Zang, J., and Hillis, A. (2014). Unsteady RANS computations of flow around a circular cylinder for a wide range of Reynolds numbers. *Ocean Engineering*, 87:1–9.

Sumer, B. and Fredsoe, J. (2006). Hydrodynamics around cylindrical structures. *Advanced Series on Ocean Engineering*, 26.

Sumner, D. (2010). Two circular cylinders in cross-flow: a review. *Journal of fluids and structures*, 26(6):849–899.

Tamura, Y. (1981). Wake-oscillator model of vortex-induced oscillation of circular cylinder. *Journal of Wind Engineering*, 1981(10):13–24.

Travin, A., Shur, M., Strelets, M., and Spalart, P. (2000). Detached-eddy simulations past a circular cylinder. *Flow, turbulence and combustion*, 63(1):293–313.

Uzun, A. and Hussaini, M. Y. (2012). An application of delayed detached eddy simulation to tandem cylinder flow field prediction. *Computers & Fluids*, 60:71–85.

Van Hinsberg, N. P. (2015). The Reynolds number dependency of the steady and unsteady loading on a slightly rough circular cylinder: From subcritical up to high transcritical flow state. *Journal of Fluids and Structures*, 55:526–539.

Weinmann, M., Sandberg, R., and Doolan, C. (2014). Tandem cylinder flow and noise predictions using a hybrid RANS/LES approach. *International journal of heat and fluid flow*, 50:263–278.

Wieselsberger, C., Betz, A., and Prandtl, L. (1923). Versuche über den widerstand gerundeter und kantiger körper. *Ergebinisse AVA Göttingen II Lieferung.*

Wilcox, D. C. (1988). Reassessment of the scale-determining equation for advanced turbulence models. *AIAA journal*, 26(11):1299–1310.

Zdravkovich, M. (1987). The effects of interference between circular cylinders in cross flow. *Journal of fluids and structures*, 1(2):239–261.

Zhang, X., Fu, S., Ong, M., and Chen, Y. (2014). Study of the flow around a cylinder from the subcritical to supercritical regimes. *Ocean Systems Engineering*, 4(3).